CHARACTERIZATION AND COMPENSATION OF PHYSIOLOGICAL FLUCTUATIONS IN FUNCTIONAL MAGNETIC RESONANCE IMAGING

A Dissertation
Presented to
The Academic Faculty

by

Jaemin Shin

In Partial Fulfillment
of the Requirements for the Degree
Doctor of Philosophy in
Bioengineering through
the School of Biomedical Engineering

Bioengineering
Georgia Institute of Technology
August 2012

CHARACTERIZATION AND COMPENSATION OF PHYSIOLOGICAL FLUCTUATIONS IN FUNCTIONAL MAGNETIC RESONANCE IMAGING

Approved by:

Dr. Xiaoping Hu, Advisor
School of Biomedical Engineering
Georgia Institute of Technology

Dr. Xiaoming Huo
School of Industrial and Systems Engineering
Georgia Institute of Technology

Dr. Shella Keilholz
School of Biomedical Engineering
Georgia Institute of Technology

Dr. Helen S. Mayberg
Department of Psychiatry and Behavioral Sciences
Emory University

Dr. John Oshinski
School of Biomedical Engineering
Georgia Institute of Technology

Date Approved: May 29, 2012

To my parents and Namin

ACKNOWLEDGEMENTS

First of all, I would like to express my deepest appreciation to my advisor, Dr. Xiaoping Hu, for his patience and support. Dr. Hu gave me freedom of my broad research interests while providing great insight whenever I lost direction. His encouragement has enriched my graduate school experience. I also would like to express profound gratitude to my committee, Dr. Xiaoming Huo, Dr. Shella Keilholz, Dr. Helen S. Mayberg, and Dr. John Oshinski for their advice and wonderful insight throughout my dissertation research.

I have been fortunate to work in the BITC. It has been amazing to interact and collaborate with BITC members. In particular, I am extremely thankful to Dr. Sinyeob Ahn, Kisueng Choi, Jihun Oh, Dr. Jaekeun Park, Dr. Qin Xu, and Dr. Zhi Yang for being wonderful friends. Additionally, I would like to thank Dr. Xiangchuan Chen, Dr. Cameron Craddock, Dr. Alex Franco, Dr. Chris Glielmi, Dr. Steve Harris, Dr. Keith Heberlein, Dr. Andy James, Dr. Steve LaConte, Dr. Jason Langley, Dr. Longchaun Li, Dr. Zhihao Li, Dr. Roger Nana, Dr. Scott Peltier, Dr. Alex Poplawski, Brenda Robledo, Dr. Priya Santhanam, Behnaz Yousefi, Dr. Lei Zhou for being so helpful and being friends.

Throughout recent years, I have also greatly benefited from the experience and support of the CABI members. The friendly and supportive atmosphere I am especially grateful to Dr. Chris Rorden, Dr. Randy Engle, Dr. Chip Epstein, Dr. Audrey Duarte, Dr. Kate Pirog Revill, Dr. Hillary Schwarb, Nytavia Wallace, Dawn Franklin, Renee Simpkins for their support and encouragement.

I thank God for bringing me into this wonderful world and wonderful people. I did not deserve to be give any of these, but you gave priceless things for no price.

I would also like to thank my church members. Special thank to Pastor Ohbyung Kwon, my spiritual father and Choi's family: Seungyeol Choi and Jiyoun Kim, my spiritual family.

Finally, by far the greatest sources of support were my family: my wife, Namin, my parents, parents-in-law, grandparents, my sisters, Jaesun and Jaehyung. The years in US helped me discover the deep love of family I was given. They have been giving me unconditional love and encouraging all the time. Namin, you have been such a wonderful wife for me and I really thank you for giving endless love and alway believing me.

TABLE OF CONTENTS

LIST OF FIGURES

SUMMARY

Functional magnetic resonance imaging (fMRI) based on blood oxygenation level dependent (BOLD) contrast has become a widespread technique in brain research. The central challenge in fMRI is the detection of relatively small activity-induced signal changes in the presence of various other signal fluctuations. Physiological fluctuations due to respiration and cardiac pulsation are dominant sources of confounding variability in BOLD fMRI. This dissertation seeks to characterize and compensate for non-neural physiological fluctuations in fMRI. First, the dissertation presents an improved and generalized technique for correcting T1 effect in cardiac-gated fMRI data incorporating flip angle estimated from fMRI dataset itself. Using an unscented Kalman filter, spatial maps of flip angle and T1 relaxation are estimated simultaneously from the cardiac-gated time series. Accounting for spatial variation in flip angle, the new method is able to remove the T1 effects robustly, in the presence of significant B1 inhomogeneity. The technique is demonstrated with simulations and experimental data. Secondly, this dissertation describes a generalized retrospective technique to precisely model and remove physiological fluctuations from fMRI signal: Physiological Impulse Response Function Estimation and Correction (PIRFECT). It is found that the modeled long-term physiological fluctuations explained significant variance in grey matter, even after removing short-term physiological effects. Finally, application of the proposed technique is observed to substantially increase the intra-session reproducibility of resting-state networks.

CHAPTER I

INTRODUCTION

The most significant and revolutionary advance in magnetic resonance imaging (MRI) in the past two decades occurred in the early 1990s when methods were developed for noninvasive mapping of brain function without the use of an exogenous contrast agent [2, 55]. Functional MRI (fMRI) has become a ubiquitously used methodology in both basic and clinical neuroscience for studying brain function in its normal and diseased states. The central challenge in fMRI is the detection of relatively small activity-induced signal changes in the presence of various non-neural fluctuations such as thermal noise, scanner related variations, subject movement, and physiological fluctuations due to the respiratory and cardiac rhythms. This dissertation encompasses efforts to characterize and reduce physiological fluctuations that interfere with fMRI studies of activation mapping, as well as functional connectivity.

1.1 BOLD fMRI

The majority of fMRI experiments are based on blood-oxygen level dependent (BOLD) contrast [61, 54, 53], which is derived from the fact that deoxyhemoglobin (dHb) in blood is paramagnetic, and change in the local concentration of dHb within the brain lead to alterations in the magnetic resonance signal [2, 55]. It is generally accepted that neuronal activation induces an increase in regional blood flow without a commensurate increase in the regional oxygen consumption rate ($CMRO_2$) [26] in which case the capillary and venous dHb concentrations should decrease, leading to an increase in T_2^*. This increase is reflected as an elevation of intensity in T_2^*-weighted

MR images. To date, fMRI has been applied to study a variety of neuronal processes, ranging from activities in the primary sensory and motor cortices to cognitive functions.

1.2 Physiological Fluctuations

A major confound in BOLD fMRI is the presence of systematic noise, which can obscure the detection of these neuronal signal changes in functional imaging data. Possible sources include (but are not limited to) signal drifts [1], physiological fluctuations due to the respiratory and cardiac rhythms [39, 30, 5, 15], and subject head motion [29]. Of these, physiological fluctuations due to respiration and cardiac pulsation are the dominant source of confounding variability in BOLD fMRI at high field strengths [39, 30, 43]. Retrospective physiological noise correction techniques [39, 30] have been introduced to reduce "short-term" effects, having instantaneous impact on fMRI signal in concert with the respiratory and cardiac processes. The physiological sources of short-term cardiac pulse effects are tissue motion, CSF motion, large vessel pulsation, and changes in blood volume in the capillary bed [39, 19]. Pulsatility of blood flow and cerebrospinal fluid (CSF) due to cardiovascular processes causes artifacts near ventricles, sulci, and large vessels [19, 30]. Large vessel pulsatility may cause tissue movement and produce an influx of unsaturated spins into the slice of interest [19]. These changes can reduce the ability to detect hemodynamic changes related to neural activity using fMRI. Retrospective correction [39, 30] has been commonly used to reduce physiological fluctuations. However, the motion of the brain itself, as well as pulsatile flow of CSF and large vessels, makes retrospective correction of cardiac noise difficult, especially in subcortical regions such as brainstem and thalamus. Short-term respiration effects result from head motion as well as B0 modulation due to bulk susceptibility changes from thoracic organ movement and gas

volume [52, 39, 58, 57, 10, 64].

However, even after removing short-term effects using the retrospective techiques [39, 30], significant correlation between fMRI change and physiological change such as cardiac rate and respiratory volume change have been observed [65, 5, 60]. Breath-to-breath variation in respiratory volume leads to fluctuations in the carbon dioxide (CO_2) content of arterial blood, a potent vasodilator. Cerebral blood flow fluctuations induced by these variations in CO_2 content result in low-frequency BOLD signal fluctuations throughout gray matter and near large vessels [65]. Respiration volume per time (RVT) has been proposed as an indicator of respiration induced signal fluctuations and has been shown to be significantly correlated with the BOLD signal [5]. These respiration induced fluctuations typically occur at a frequency of approximately 0.03 Hz [65, 5]. In addition, significant correlations between cardiac rate and BOLD signal fluctuations have been reported [60, 15]. While variations in respiration depth, respiration rate and heart rate are examples of sources of long-term effects, there are potentially other sources that have yet to be identified.

1.3 Functional Connectivity and Resting-State Networks

Along with the rapid growth of methods and applications of functional brain mapping for localizing regions with specialized functions, there has been a great deal of interest and progress made in studying brain connectivity. In particular, neuroimaging data can be used to infer functional connectivity which permits a systematic understanding of brain activity and allows the establishment and validation of network models of various brain functions. With the advent of functional neuroimaging, approaches have been developed to probe functional connectivity [44]. One approach for examining connectivity, that has gained a great deal of interest, is based on the

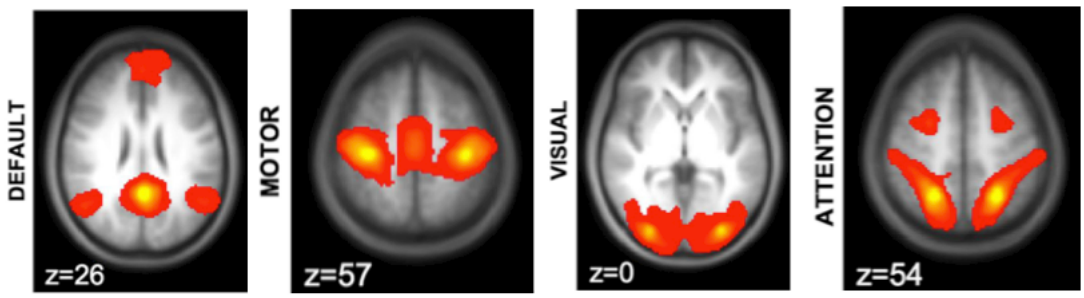

Figure 1: Examples of resting-state networks adapted from Van Dijk et al. [63]. Images were obtained using seed-based correlation for regions within default, motor, visual, and attention networks.

temporal correlations in functional neuroimaging data [27]. Functional connectivity has been defined as "temporal correlations between spatially remote neurophysiological events [27]." With fMRI data acquired during the absence of an explicit task, i.e., the resting-state, low-frequency time course fluctuations were found to be temporally correlated between functionally related areas. These low frequency oscillations seem to be a general property of symmetric cortices and/or relevant regions, have been shown to exist in a number of brain networks [36, 8, 9, 48] and have been revealed with data-driven analysis approaches [18, 56]. These fluctuations agree with the concept of functional connectivity defined by Friston et al. [27]. Examples of such resting-state networks (RSNs) include visual, motor, and attention networks, as well as default-mode network as depicted in Fig. 1.

Several signal-processing techniques may be employed to delineate functional connectivity [45]. Of these, seed-based correlation and independent component analysis (ICA) exemplify two of the most frequently-used classes of methods. In seed-based

correlation, one computes an index of temporal similarity such as Pearson correlation between one region of interests (ROI) and all other voles in the brain [32, 8]. Other techniques have been proposed for resting-state network such as independent component analysis (ICA) [4] and self-organizing maps [56].

Long-term physiological effects are particularly detrimental in resting-state functional connectivity analysis since their frequency range overlaps with the frequencies of fluctuations believed to reflect resting brain activity. Recent studies have shown significant correlations between the long-term physiological signal change and fMRI throughout gray matter, impeding detection of resting-state networks [6, 16]. Furthermore, studies have shown that the spatial distribution of the respiration long-term effects coincide with the default mode network [6].

CHAPTER II

CORRECTION FOR T1 EFFECT INCORPORATING FLIP ANGLE ESTIMATED BY KALMAN FILTER IN CARDIAC-GATED FMRI

2.1 Introduction

The central challenge in functional magnetic resonance imaging (fMRI) is the detection of relatively small activity-induced signal changes (<3%) in the presence of various other signal fluctuations. Pulsatility of blood flow and cerebrospinal fluid (CSF) due to cardiovascular processes causes artifacts near ventricles, sulci, and large vessels [19, 30]. Large vessel pulsatility may cause tissue movement and produce an influx of unsaturated spins into the slice of interest [19]. These changes can reduce the ability to detect hemodynamic changes related to neural activity using fMRI. Retrospective correction [39, 30] has been commonly used to reduce physiological fluctuations. However, the motion of the brain itself, as well as pulsatile flow of CSF and large vessels, makes retrospective correction of cardiac noise difficult, especially in subcortical regions such as brainstem and thalamus.

To overcome this problem, cardiac-gated acquisition has been introduced as a means to freeze pulsation-induced brain movement [34]. The primary difficulty with this strategy lies in the TR inconsistency due to the variation of the cardiac cycle. This TR variability introduces T1 related signal fluctuations (denoted "T1 effect", approximately 7% with a TR that has a 10% variation around 1 s, T1 = 1600 ms and flip angle = 90° for gray matter), which may overwhelm the BOLD signal change (<

3%). A passive approach to avoid this variation is to use a TR long enough (e.g. 9 - 10 s) to reach nearly full T1 relaxation in each measurement [33]. However, such an approach inevitably sacrifices temporal resolution. A processing technique previously introduced previously for correcting T1 effect [21, 34] is effective but only valid for the flip angle of 90°. B1 inhomogeneity can often cause the significant variation of a flip angle, e.g., 65° to 105° over the entire brain for the nominal flip angle of 90° at 3T [40, 50]. In the presence of such spatial inhomogeneity, the existing technique is not effective for correcting T1 variation over the entire volume of brain even for the nominal flip angle of 90°. Moreover, when a nominal flip angle less than 90° such as the Ernst angle is used, the existing correction technique is also inappropriate.

In this chapter, I describe an improved and generalized technique for correcting T1 effect in cardiac-gatedh fMRI data incorporating flip angle estimated from fMRI dataset itself. Using an unscented Kalman filter [41], spatial maps of flip angle and T1 relaxation are estimated simultaneously from the cardiac-gated time series. These maps are subsequently used for removing the T1 effects in the fMRI data. The robustness of this new approach is demonstrated with simulated and experimental data.

2.2 Theory

2.2.1 MR Signal Model

In a gated fMRI run, the longitudinal magnetization signal before the k^{th} RF pulse is applied, $M_z^-(k)$, is decried by [35]:

$$M_z^-(k) = (\cos\alpha) M_z^-(k-1)\, e^{-\frac{\mathrm{TR}_k}{\mathrm{T1}}} + M_0 \left[1 - e^{-\frac{\mathrm{TR}_k}{\mathrm{T1}}}\right] \tag{1}$$

where M_0 is the equilibrium magnetization, TR is a repetition time, α is the nominal flip angle, and k denotes the time point. Then, the transverse magnetization, $M_{xy}(k)$, obtained by multiplying $\sin\alpha$ in the both sides of Eg. (1), noting that $M_{xy}(k) = M_z^-(k)\sin\alpha$, is

$$M_{xy}(k) = (\cos\alpha) M_{xy}(k-1)\, e^{-\frac{\mathrm{TR}_k}{\mathrm{T1}}} + M_0 \sin\alpha \left[1 - e^{-\frac{\mathrm{TR}_k}{\mathrm{T1}}}\right]. \tag{2}$$

The MR signal for the k^{th} time point, $m_k \triangleq M_{xy}(k) e^{-\frac{\mathrm{TE}}{\mathrm{T2}_k^*}}$ becomes

$$m_k = (\cos\alpha) M_{xy}(k-1)\, e^{-\frac{\mathrm{TE}}{\mathrm{T2}_k^*}} e^{-\frac{\mathrm{TR}_k}{\mathrm{T1}}} + M_0 (\sin\alpha)\, e^{-\frac{\mathrm{TE}}{\mathrm{T2}_k^*}} \left[1 - e^{-\frac{\mathrm{TR}_k}{\mathrm{T1}}}\right] \tag{3}$$

$$= (\cos\alpha)\, m_{k-1}\, e^{\left(\frac{\mathrm{TE}}{\mathrm{T2}_{k-1}^*} - \frac{\mathrm{TE}}{\mathrm{T2}_k^*}\right)} e^{-\frac{\mathrm{TR}_k}{\mathrm{T1}}} + M_0 (\sin\alpha)\, e^{-\frac{\mathrm{TE}}{\mathrm{T2}_k^*}} \left[1 - e^{-\frac{\mathrm{TR}_k}{\mathrm{T1}}}\right]. \tag{4}$$

While the T2* term, $e^{-\frac{\mathrm{TE}}{\mathrm{T2}_k^*}}$, is time-varying, mostly owning to the BOLD contrast, we assumed this variation negligible such that $e^{\left(\frac{\mathrm{TE}}{\mathrm{T2}_{k-1}^*} - \frac{\mathrm{TE}}{\mathrm{T2}_k^*}\right)}$ can be set to 1, for the purpose of estimating the flip angle and T1, because the BOLD signal varies slowly [13]. With this approxiamation, the MR signal is given by

$$m_k = (\cos\alpha) m_{k-1}\, e^{-\frac{\mathrm{TR}_k}{\mathrm{T1}}} + M_0 (\sin\alpha) e^{-\frac{\mathrm{TE}}{\mathrm{T2}_k^*}} \left[1 - e^{-\frac{\mathrm{TR}_k}{\mathrm{T1}}}\right]. \tag{5}$$

2.2.2 T1 Only Correction

For the special case of α being 90°, the MR signal given by Eq. (5) is simplified to

$$m_k = M_0\, e^{-\frac{\mathrm{TE}}{\mathrm{T2}^*_k}} \left[1 - e^{-\frac{\mathrm{TR}_k}{\mathrm{T1}}}\right] \tag{6}$$

In conventional ungated acquisition (e.g. $\mathrm{TR}_k = 2$ sec), the T1-dependent signal term, $1 - e^{-\frac{\mathrm{TR}_k}{\mathrm{T1}}}$ is constant while the T2*-dependent signal term provides the signal contrast of interest. However, in cardiac-gated acquisition, MR signal is also modulated by the T1-dependent term due to the variation of a cardiac cycle. This T1 effect may overwhelm the T2* signal change. Correction techniques for this T1 effect were developed for the special case of α being 90° [21, 34]. With measurements with TR of 20 sec and 1 sec, one can estimate the T1, assuming that TR of 20 sec allows full T1 signal recovery [21]. With estimated $\hat{\mathrm{T1}}$ and average TR, the correction is made by multiplying the following correction term:

$$m_{k,cor} = m_k \left[\frac{1 - e^{-\mathrm{TR}_{avg}/\hat{\mathrm{T1}}}}{1 - e^{-\mathrm{TR}_k/\hat{\mathrm{T1}}}}\right]. \tag{7}$$

In the presence of spatial inhomogeneity of B1, this correction is not valid over the entire volume of brain even for the nominal flip angle of 90°

2.2.3 T1 Correction with Flip Angle Estimation

In this study, I describe a generalized technique for correcting T1 effect taking into account the actual flip angle. I first estimated the flip angle and the T1. Unscented Kalman filter, a recursive minimum mean square error (MMSE) estimator based on the optimal Gaussian approximate Kalman filter framework [62], is used to simultaneously estimate the T1 and the flip angle from fMRI time series. Kalman filter

has been widely used for nonlinear estimation including the estimation of the state of a nonlinear dynamic system, such as fMRI time series [37]. The basic framework for Kalman filtering involves the estimation of the state of a discrete-time dynamic system described in a state-space model,

$$\mathbf{S}_k = f\left(\mathbf{S}_{k-1}, \mathbf{v}_k\right) \tag{8}$$

$$y_k = h\left(\mathbf{S}_k, w_k\right), \tag{9}$$

where $\mathbf{S}_k$ represents the state random variable of the system and y_k is the measured signal. The state and measurement noises are given by $\mathbf{v}_k$ and w_k, respectively. The system dynamic models, $f(\cdot)$ and $h(\cdot)$, are assumed known. The Kalman filter involves the recursive estimation of the mean and covariance of the state and consists of two steps, prediction followed by update [42]:

$$\begin{aligned} \hat{\mathbf{S}}_k &= (\text{prediction of } \mathbf{S}_k) + \mathbf{K}_k \left(y_k - (\text{prediction of } y_k)\right) \\ &= \hat{\mathbf{S}}_k^- + \mathbf{K}_k \left(y_k - \hat{y}_k^-\right) \\ \mathbf{P}_{\mathbf{S}_k} &= \mathbf{P}_{\mathbf{S}_k}^- - \mathbf{K}_k \mathbf{P}_{\tilde{y}_k} \mathbf{K}_k^T, \end{aligned} \tag{10}$$

where $\mathbf{K}_k$ denotes the optimal Kalman gain, the optimal predictions of $\mathbf{S}_k$ and y_k are written as $\hat{\mathbf{S}}_k^-$ and $\hat{y}_k^-$ respectively and the covariance matrix is represented as $\mathbf{P}$. The

optimal terms in this recursion for a given system are expressed by

$$\begin{aligned}
\hat{\mathbf{S}}_k^- &= \mathbb{E}\left[f(\mathbf{S}_{k-1}, \mathbf{v}_k)\right] \\
\hat{y}_k^- &= \mathbb{E}\left[h(\mathbf{S}_k^-, w_k)\right] \\
\mathbf{K}_k &= \mathbb{E}\left[(\mathbf{S}_k - \hat{\mathbf{S}}_k^-)(y_k - \hat{y}_k^-)^T\right]\mathbb{E}[(y_k - \hat{y}_k^-)(y_k - \hat{y}_k^-)^T]^{-1} \\
&= \mathbf{P}_{\mathbf{S}_k \tilde{y}_k}\, \mathbf{P}_{\tilde{y}_k}^{-1},
\end{aligned} \tag{11}$$

where $\hat{\mathbf{S}}_k^-$ and $\hat{y}_k^-$ are the expectation values of the corresponding random variables and $\tilde{y}_k$ is the prediction error (or innovation, $y_k - \hat{y}_k^-$). The Kalman gain $\mathbf{K}_k$ is expressed as a function of the expected cross-covariance matrix of the state prediction error and the measurement prediction error, and the expected auto-correlation matrix of the measurement prediction error. The optimal solution for Kalman filter requires taking expectations of a nonlinear function of a state variable, which can be approximated by an unscented transformation. The unscented transformation is a method to propagate the statistics of a random variable through nonlinear transformations and builds on the principle that *it is easier to approximate probability distributions than it is to approximate an arbitrary nonlinear function or transformation* [41]. Please refer to the Appendix for details on unscented transformation and unscented Kalman filter.

Now we put the MR signal model given in Eq. (5) into the Kalman filter framework. The random state variable $\mathbf{S}_k$ consists of flip angle, T1, T2* signal change, and MR

signal at the k^{th} time point:

$$\mathbf{S}_k = \begin{bmatrix} s_{k,1} \\ s_{k,2} \\ s_{k,3} \\ s_{k,4} \end{bmatrix} = \begin{bmatrix} \alpha \\ \mathrm{T1} \\ M_0(\sin\alpha)e^{-\frac{\mathrm{TE}}{\mathrm{T2}^*_k}} \\ m_k \end{bmatrix}. \tag{12}$$

The MR signal time-series in Eq. (5) is represented as a state-space model, $\mathbf{S}_k = f(\mathbf{S}_{k-1}, \mathbf{v}_k)$:

$$\begin{aligned} s_{k,1} &= s_{k-1,1} + v_{k,1} \\ s_{k,2} &= s_{k-1,2} + v_{k,2} \\ s_{k,3} &= s_{k-1,3} + v_{k,3} \\ s_{k,4} &= s_{k-1,4}\cos(s_{k,1})\; e^{-\frac{\mathrm{TR}_k}{s_{k,2}}} + s_{k,3}\left[1 - e^{-\frac{\mathrm{TR}_k}{s_{k,2}}}\right], \end{aligned} \tag{13}$$

where $\mathbf{v}_k = [v_{k,1}, v_{k,2}, v_{k,3}]^T$ is a random Gaussian state noise, $\mathbf{v}_k \sim \mathbf{N}(\mathbf{0}, \mathbf{P}_{\mathbf{v_k}})$. It is noted that T1 and the flip angle are modeled as random variables, allowing the propagation of model mismatch through nonlinear functions, such as the exponential term and cosine term in the MR signal model. The measured signal y_k is described as:

$$y_k = h(\mathbf{S}_k, w_k) = s_{k,4} + w_k \tag{14}$$

where w_k denotes a random Gaussian measurement noise, $w_k \sim \left(0, \sigma^2_{w_k}\right)$.

Once the flip angle and the T1 is estimated as $\hat{\mathrm{T1}}$ and $\hat{\alpha}$, the T2*-dependent signal term, $M_0(\sin\alpha)e^{-\frac{\mathrm{TE}}{\mathrm{T2}^*_k}}$ is estimated using two consecutive fMRI measurements

from Eq. (5) by

$$M_0(\sin\alpha)e^{-\frac{\mathrm{TE}}{\mathrm{T2}^*_k}} = \frac{m_k - m_{k-1}(\cos\hat{\alpha})e^{-\mathrm{TR}_k/\hat{\mathrm{T1}}}}{1 - e^{-\mathrm{TR}_k/\hat{\mathrm{T1}}}}. \tag{15}$$

Then, the corrected time series is generated using the general MR signal model given by Eq. (5) as follows:

$$m_{k,cor} = (\cos\hat{\alpha})m_{k-1,cor}\, e^{-\frac{\mathrm{TR}_{avg}}{\hat{\mathrm{T1}}}} + M_0(\sin\alpha)e^{-\frac{\mathrm{TE}}{\mathrm{T2}^*_k}}\left[1 - e^{-\frac{\mathrm{TR}_{avg}}{\hat{\mathrm{T1}}}}\right]. \tag{16}$$

2.3 Methods

2.3.1 Simulation

Simulated cardiac-gated fMRI time series were generated from Eq. (5) for a range of flip angles ($60^\circ \sim 110^\circ$) and T1s (800 ms $\sim$ 2000 ms) with the addition of T2* related change (3%) and timing information of the experiment described below. TR variation was based on actual scan parameters from a representative participant. Noise was generated and added in such a way that a temporal SNR (tSNR) is 90 with a mixture of 70% white noise and 30% first-order autoregressive noise [28]. Corrections for T1 effect were performed using "T1 only" and the "T1 & flip angle" methods. The performance of correction was evaluated using tSNR, calculated by dividing the mean of a time series by the standard deviation of its corrected version.

2.3.2 Experimental Design

Data Acquisition

Seven healthy volunteers participated in the experimental study after giving informed consent in accordance with Emory University's institutional review board. All MRI

experiments were conducted on a 3T Siemens Tim Trio scanner (Siemens Medical Solutions, Malvern, PA) equipped with a twelve-channel head coil. Anatomic images were acquired with a 3D T1-weighted magnetization-prepared rapid gradient echo imaging (MPRAGE) sequence (FOV = 256×256×176 mm^3, resolution 1×1×1 mm^3, TR = 2250 ms, TE = 2.52 ms, flip angle = 9°). Each subject subsequently underwent two randomly ordered fMRI scans, an ungated scan and a gated scan. All functional scans were acquired using a T2*-weighted echo-planar imaging sequence with the following parameters: 270-volumes, FOV = 220 × 220 mm^2, matrix = 110 × 110, 8 ascending axial slices with 20 % gap, thickness = 3 mm, TE = 30 msec, generalized auto-calibrating partially parallel acquisition (GRAPPA) imaging with an acceleration factor of 2. For the gated scan, TR was determined by each subject's heart rate. The average heart rate of each subject was used to determine the TR for the ungated scan to match the total scan time as well as the number of volumes. In addition, two volumes were collected with the same parameter as functional scan except with TR = 1 sec and 20 sec used to calculate T1 for the "T1 only" method. To inspect a registration result between the partial coverage of the functional scan and the whole brain anatomical scan, two sets of 2D T1-weighted anatomical images were also collected on slices of the functional scans, one with the partial coverage same as the functional scan and the other with the whole brain coverage.

Physiological Recording

All physiological recording was performed using an integrated Siemens Physiological Monitoring Unit. During functional scans, the cardiac signal was monitored with a pulse oximeter placed on a finger of subjects, which provides a delayed systolic signal as well as the oxygenation saturation level. Respiratory signal was monitored with a flexible pressure belt placed around the upper abdomen of subjects. The sampling

frequency of all physiological recording was 50 Hz.

Task Design

A central fixation cross was presented continuously and subjects were instructed to gaze at the cross during fMRI scans (30 TRs of rest). Each fMRI scan started with 30 TRs of rest, followed by four set of 30 TRs of visual stimulation and 30 TRs of rest. An inverting half-filled checkerboard alternated between left and right hemifields at 8Hz during the visual stimulation. Visual stimuli were generated by an LCD projector, back-projected onto a screen mounted at the rear of a scanner bore, and viewed through a mirror mounted on the head coil.

Data Analysis

For each subject, 4 types of time series were derived from the two scans: (1) ungated scan; (2) gated scan with no correction; (3) gated scan with the "T1 only" correction; and (4) gated scan with the "T1 & flip angle" correction. AFNI (`http://afni.nimh.nih.gov/afni/`) was used for most of the data analysis. In addition, FSL (`http://www.fmrib.ox.ac.uk/fsl/`) was used for brain segmentation and registration. The "T1 & flip angle" correction was performed using Matlab (MathWorks, Natick, MA) routines with ReBEL Matlab toolbox (`http://choosh.csee.ogi.edu/rebel/`) for unscented Kalman filter. The first ten volumes of each run were discarded to remove T1 saturation effects. Remaining volumes underwent motion correction, linear detrending, and spatial smoothing (full width of half maximum (FWHM) = 3 mm). Retrospective correction [30] was performed to reduce respiration effect for all time-series and cardiac effect for ungated time series.

A multiple regression analysis was performed in the native space of each individual subject. Regressors represent the two visual stimulation conditions (left and right stimulus) and their temporal derivatives, were used to derive subject-level activation maps which reflect the contralateral response of the visual system. To compare temporal characteristics, tSNR was calculated from the standard deviation of the residual time series produced by the regression analysis for each voxel. The regression coefficients were registered to a standard space using FSL's nonlinear image registrations tool (FNIRT) and fed into a one-sample t-test for group level activation maps. The effect of different corrections on the activation was further examined by a regions of interest (ROI) analysis. Two ROIs were functionally defined; one in the subcortical region (the lateral geniculate nucleus (LGN)) and the other in the cortical region (visual cortex) based on the group activation maps ($p < 0.01$, uncorrected). Specifically, LGN activations were identified from contiguous voxels in the anatomical location of the LGN from the AFNI atlas. Visual cortex activations were restricted to Brodmann areas 17 and 18. Finally, one common ROI was created by taking an inclusive union of activated voxels across 4 different approaches for each ROI.

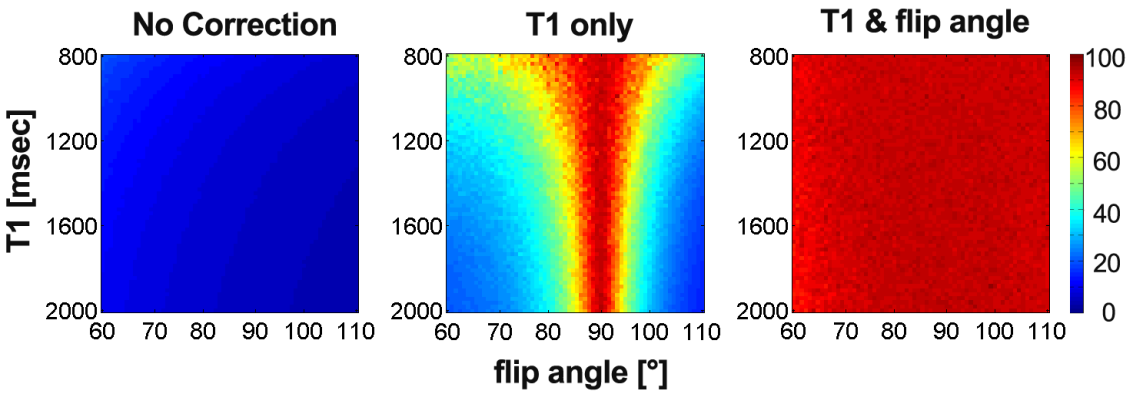

Figure 2: Temporal SNR in simulated time series for varying flip angle and T1.

2.4 Results

Figure 2 shows tSNR map in the simulated time series as a function of the flip angles ($60° \sim 110°$) and T1s (800 ms $\sim$ 2000 ms). While tSNR values in the "T1 only" correction show a significant increase only around the flip angle of 90°, tSNR values in the "T1 & flip angle" correction exhibit an increase across the entire range of flip angles tested. This clearly indicates that the "T1 only" correction is effective only the actual flip angle is near 90°.

The percentage changes in tSNR using the two correction methods for the gated time series relative to the ungated time series are presented in Fig. 3. The increase of tSNR was observed in subcortical regions including LGN and brain stem for both correction methods compared to the ungated time series, as a result of cardiac-gated acquisition. For the "T1 only" correction, the gain comes at the expense of substantial decrease of tSNR in grey matter while the "T1 & flip angle" correction did not result in the reduction of tSNR in grey matter. The tSNR was averaged across grey matter for all participants (Fig. 4). The result from the gated times series with the "T1 & flip

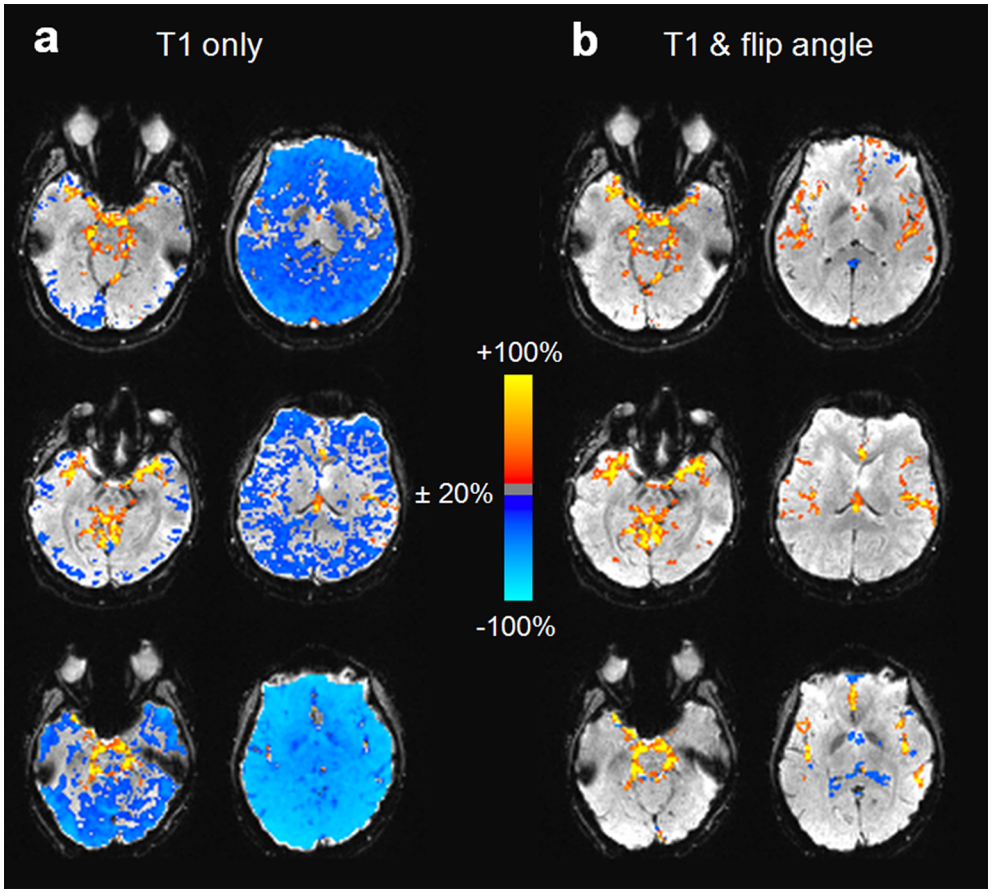

Figure 3: Changes in tSNR for the gated time series with (a) "T1 only" correction and (b) "T1 & flip angle" correction compared to the conventional ungated time series for 3 subjects.

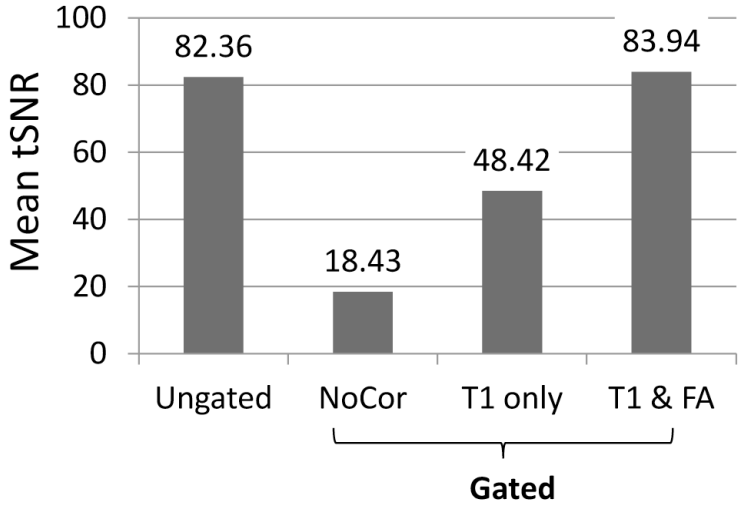

Figure 4: Grey matter tSNR, averaged from 7 subjects of the ungated time series and gated time series with different correction methods

angle" correction was significantly higher than those from the "T1 only" correction across subjects (a paired t-test $p < 0.004$). This indicates that the new correction improved the temporal signal stability by reducing signal fluctuations induced by variable TRs.

Representative time series from *in vivo* data are presented in Fig. 5. It is evident that fluctuations are substantially more reduced by the "T1 & flip angle" correction compared to the "T1 only" correction while the contrast of interest remains unaffected. Time courses from a representative subject are illustrated in Fig. 6. The estimated flip angle shows a wide variation, ranging from 62° to 95° consistent with previous reports [50, 40]. Activation results clearly demonstrate that the "T1 & flip angle" correction is superior over the "T1 only" correction in terms of statistical significance and spatial extent in left visual cortex for a right stimulus condition.

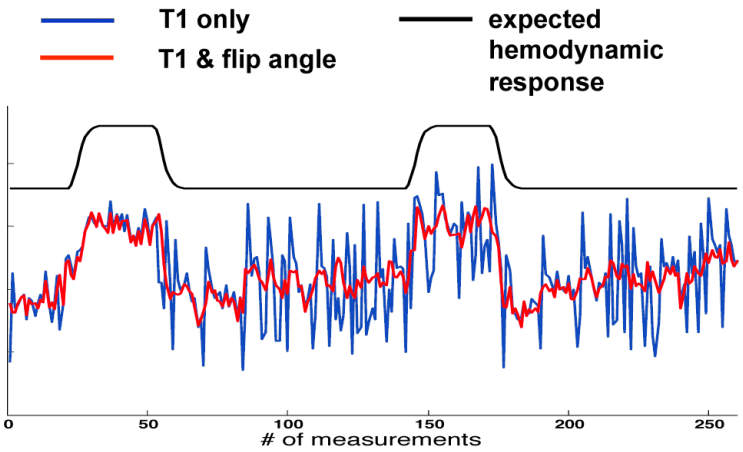

Figure 5: Time courses in a representative voxel in the right visual cortex derived from two different correction methods (T1 only vs T1 & flip angle)

To further examine the activations in the two ROIs, we first compared the number of activated voxels at the group level analysis. Figure 6 demonstrates that the number of activated voxels in the LGN from both correction methods for the dated time series (75 voxels for the "T1 only" and 79 voxels for the "T1 & flip angle") is higher than that of the ungated dataset (40 voxels). Gated time series with no correction did not show any LGN activation at the group level analysis. The result indicates that the gated fMRI acquisition with the correction approaches is effective at increasing signal detection in the LGN. The effectiveness of the correction for T1 effect was further assessed in terms of its impact on the statistics at the subject level analyses. The t-statistic maps were converted to Z-statistics and the mean Z-statistics across subjects for different approaches were compared. The values derived from the "T1 & flip angle" correction are significantly higher than those of the "T1 only" correction across all subjects according to a paired t-test ($p < 0.002$), indicating that the new correction improved statistical detection. In the visual cortex, there is no significant difference between the ungated approach and the "T1 & flip angle" approach in term

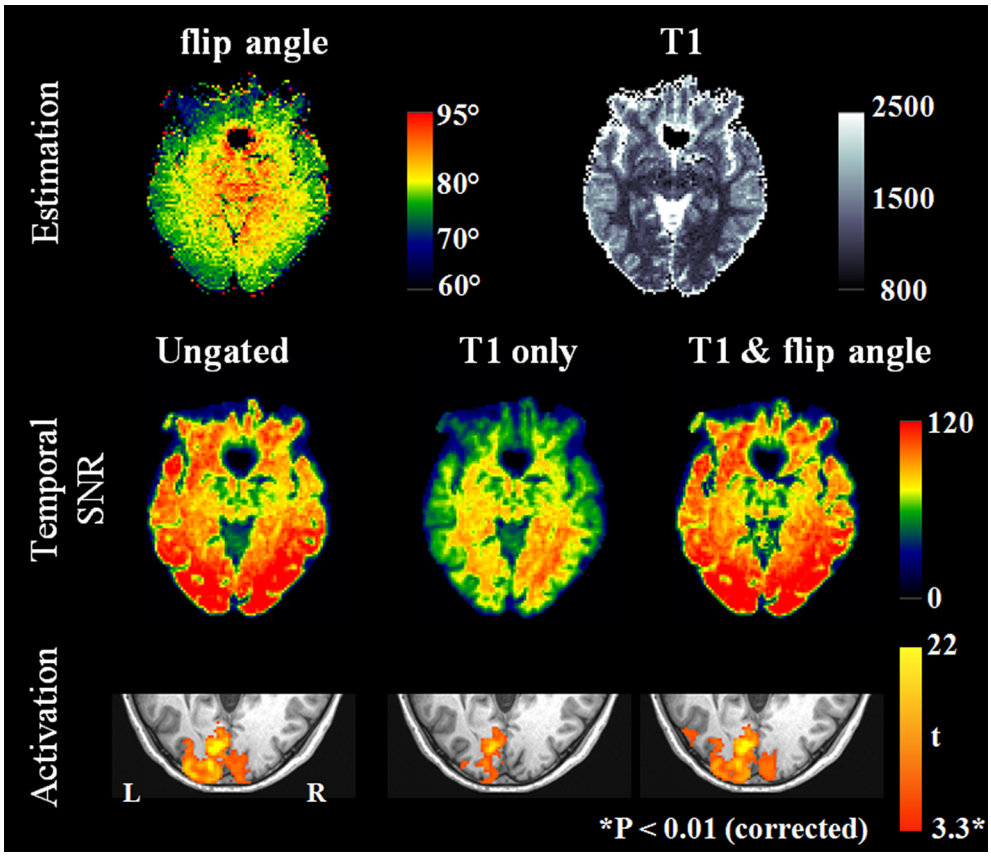

Figure 6: Results from a representative subject: (top) estimated flip angle and T1 using Kalman filter, (middle) tSNR maps, and (bottom) activation maps for the right field stimulus at $p < 0.05$ (corrected).

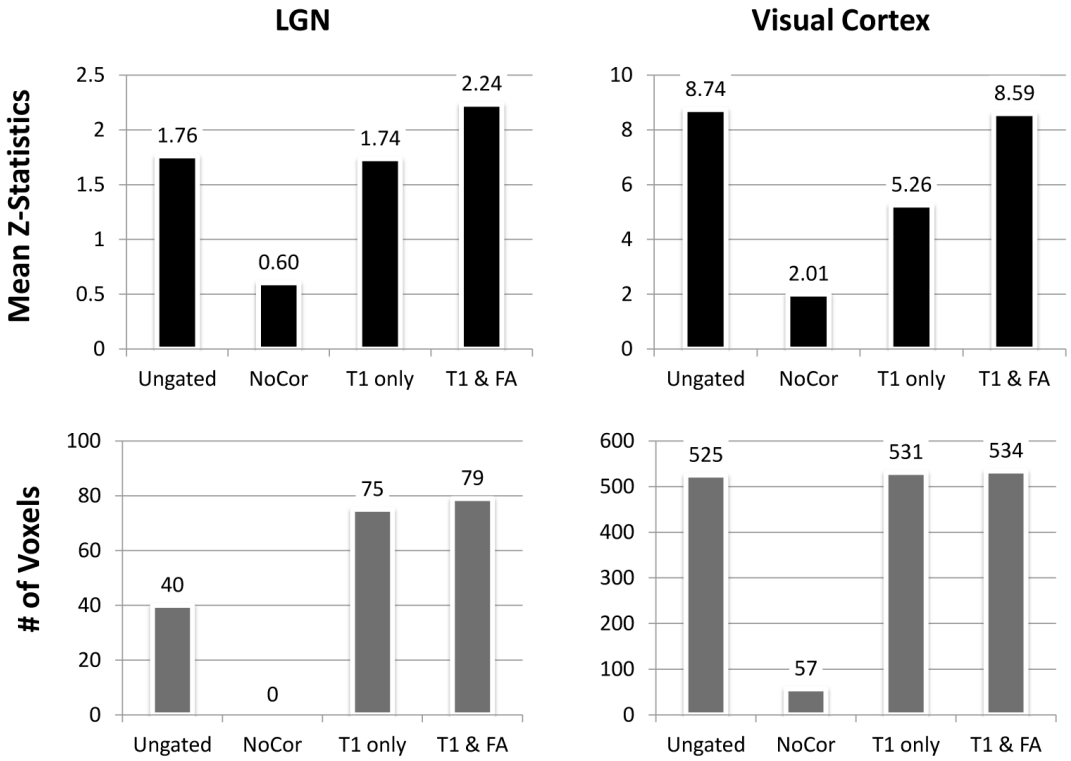

Figure 7: Comparison of the activations in LGN and visual cortex ROIs for four different time series: (top) mean Z-statistics and (bottom) the number of activated voxels ($p < 0.01$, uncorrected).

of the number of activated voxels and the mean Z-statistics. However, the "T1 only" approach led to a mean Z-score that only 60 % of those obtained with the ungated approach and the "T1 & flip angle" approach demonstrating that the "T1 only" approach redues the detection power in the visual cortex, due to the use of incorrect flip angle.

2.5 Discussion

This work introduces a more general technique, which accounts for spatial variation in flip angle, for correcting T1 effect in cardiac-gated fMRI. The new method removes T1 related signal fluctuations throughout the entire brain in the presence of B1 inhomogeneity. Cardiac-gated fMRI has been shown to improve the sensitivity of fMRI, particularly for subcortical regions because they tend to move more with cardiac pulsation. Experimental results reported here demonstrated the improved detection of LGN activation with gated acquisition and T1 correction. However, the gain in the subcortical region by the "T1 only" is associated with a loss of sensitivity in the cortex due to the use of incorrect flip angle in the presence of B1 inhomogeneity. This loss of sensitivity is clearly seen in simulation and experimental data, particularly in the lower statistics values (5.26) in the visual cortex activation derived with "T1 only" compared to that of the ungated (8.74). As demonstrated by simulation and experimental results, "T1 & flip angle" approach introduced in this work completely eliminated this loss of sensitivity and made the gated acquisition more robust.

It is challenging to study subcortical nuclei using fMRI because of their small sizes, relatively low BOLD contrast, and deep locations susceptible to pulsatile motion artifacts. From our results in this study, the hemifield retinotopic relationship in the human brain was demonstrated in the LGN, the thalamic station in the projection of

the visual pathway from retina to primary visual cortex. These results are consistent with earlier observations [59, 17]. Thus, cardiac-gated fMRI with the correction technique developed here offer opportunities for studying subcortical regions without the compromise of reducing the detection power in cortical regions.

The new approach does not require additional scans to estimate the flip angle and T1. The natural variability of TR in the gated fMRI allows the estimation of the parameters directly from the acquired data using Kalman filter. The technique of estimating the flip angle using Kalman filter may be be utilized in other applications where a flip angle (or B1) map is needed. It is also worth noting that Kalman filter can be also used to estimate the T2* change, $s_{k,3}$ in Eq. (12), from noisy fMRI measurements as the unobserved time-varying state estimation. We have used Kalman filter for estimating the flip angle and T1 as unknown constants in this study. In state estimation method, Kalman filter eliminates not only T1 effect, but also the measurement noise, which would result in better tSNR. However, caution should be exercised as the neural activity-related signal can be confounded with the measurement noise in Kalman filter.

2.6 Conclusions

A technique for correcting T1 effects in cardiac-gated fMRI data is presented here. Accounting for spatial variation in flip angle, the new method is able to remove the T1 effects robustly, in the presence of significant B1 inhomogeneity. The technique is demonstrated with simulations and experimental data. Therefore, the technique is expected to be a promising tool for improving the ability of mapping activation in fMRI,especially in subcortical regions.

2.7 Acknowledgements

This work was supported in part by the National Institutes of Health (R01EB002009) and Georgia Research Alliance.

2.8 Appendix

2.8.1 Unscented Transformation

We consider the propagation of an L dimensional random variable $\mathbf{X}$ through an arbitrary nonlinear function,

$$\mathbf{Y} = g(\mathbf{X}) \tag{17}$$

Assume $\mathbf{X}$ has mean $\bar{\mathbf{X}}$ and covariance matrix $\mathbf{P_X}$. We define a set of 2L+1 weighted samples, called sigma points $\{w^{(i)}, \mathbf{X}^{(i)}\}$ are deterministically chosen so that they completely capture the true mean and covariance of the prior random variable $\mathbf{X}$ as follows:

$$\begin{aligned}
&\mathbf{X}^{(0)} = \bar{\mathbf{X}} && w^{(0)} = 1/L && i = 0 \\
&\mathbf{X}^{(i)} = \bar{\mathbf{X}} + \left(\sqrt{L\mathbf{P_X}}\right)^{(i)} && w^{(i)} = 1/2L && i = 1, \ldots, L \\
&\mathbf{X}^{(i)} = \bar{\mathbf{X}} - \left(\sqrt{L\mathbf{P_X}}\right)^{(i)} && w^{(i)} = 1/2L && i = L+1, \ldots, 2L.
\end{aligned} \tag{18}$$

Each sigma point is now propagated through the nonlinear function

$$\mathbf{Y}^{(i)} = f(\mathbf{X}^{(i)}) \qquad i = 0, \ldots, 2L \tag{19}$$

and the approximated mean, covariance and cross-covariance of $\mathbf{Y}$ are computed as follows:

$$
\begin{aligned}
\bar{\mathbf{Y}} &\approx \sum_{i=0}^{2L} w^{(i)} \mathbf{Y}^{(i)} \\
\mathbf{P}_{\mathbf{Y}} &\approx \sum_{i=0}^{2L} w^{(i)} \left(\mathbf{Y}^{(i)}) - \bar{\mathbf{Y}}\right) \left(\mathbf{Y}^{(i)} - \bar{\mathbf{Y}}\right)^T \\
\mathbf{P}_{\mathbf{XY}} &\approx \sum_{i=0}^{2L} w^{(i)} \left(\mathbf{X}^{(i)} - \bar{\mathbf{X}}\right) \left(\mathbf{Y}^{(i)} - \bar{\mathbf{Y}}\right)^T
\end{aligned}
\tag{20}
$$

These estimates are accurate to the second order (third order for true Gaussian priors) for any nonlinear functions [62]. Now, we apply the unscented transformation to the recursive Kalman filter framework.

2.8.2 Unscented Kalman Filter

The unscented transformation is used to approximate the optimal terms in Eq. (11) where the state random variable is redefined as the concatenation of the original state and the process and observation noise random variables. By augmenting the state random variable with the noise random variables as shown in Eq. (21), we take the uncertainty in the noise random variables into account in the same manner as we do for the state during the sigma point propagation.

$$
\mathbf{S}_{a,k} = \begin{bmatrix} \mathbf{S}_k & \mathbf{v}_k & \mathbf{w}_k \end{bmatrix}^T \quad \mathbf{P}_{\mathbf{S}_{a,k}} = \begin{bmatrix} \mathbf{P}_{\mathbf{S}_k} & 0 & 0 \\ 0 & \mathbf{P}_{\mathbf{S}\mathbf{v}_k} & 0 \\ 0 & 0 & \mathbf{P}_{w_k} \end{bmatrix} \tag{21}
$$

The unscented Kalman filter is summarized as follows [41]:

1) The set of sigma points is calculated by Eq. (18) based on augmented state random variable as Eq. (21).

2) The transformed set is given through the MR signal model, $f(\cdot)$ given by Eq. (13):

$$\mathbf{S}^{(i)}_{a,k|k-1} = f(\mathbf{S}^{(i)}_{a,k-1}). \tag{22}$$

3) The predicted mean and covariance is computed as

$$\begin{aligned} \hat{\mathbf{S}}^{-}_{a,k} &= \sum_{i=0}^{2L} w_k^{(i)}\, \mathbf{S}^{(i)}_{a,k|k-1} \\ \mathbf{P}^{-}_{\mathbf{s}_{a,k}} &= \sum_{i=0}^{2L} w_k^{(i)} \left(\mathbf{S}^{(i)}_{a,k|k-1} - \hat{\mathbf{S}}^{-}_{a,k}\right) \left(\mathbf{S}^{(i)}_{a,k|k-1} - \hat{\mathbf{S}}^{-}_{a,k}\right)^T. \end{aligned} \tag{23}$$

4) Each of the prediction points is instantiated through the measurement model, Eq. (14):

$$y^{(i)}_{k|k-1} = h\left(\mathbf{S}^{(i)}_{a,k|k-1}\right) = s^{(i)}_{k|k-1,4}. \tag{24}$$

5) The predicted measurement, the innovation, covariance matrix, and the cross covariance matrix are calculated by

$$\begin{aligned} \hat{y}^{-}_k &= \sum_{i=0}^{2L} w_k^{(i)}\, y^{(i)}_{k|k-1} \\ \mathbf{P}_{\tilde{y}_k} &= \sum_{i=0}^{2L} w_k^{(i)} \left(y^{(i)}_{k|k-1} - \hat{y}^{-}_k\right)^2 \\ \mathbf{P}_{\mathbf{s}_k \tilde{y}_k} &= \sum_{i=0}^{2L} w_k^{(i)} \left(\mathbf{S}^{(i)}_{k|k-1} - \mathbf{S}^{-}_k\right) \left(y^{(i)}_{k|k-1} - \hat{y}^{-}_k\right)^T, \end{aligned} \tag{25}$$

where the innovation $\tilde{y}_k$ is the measurement prediction error.

6) The Kalman gain is calculated by

$$\mathbf{K}_k = \mathbf{P}_{\mathbf{s}_k, \tilde{y}_k} \mathbf{P}^{-1}_{\tilde{y}_k}. \tag{26}$$

7) Finally, the update can be performed using the Kalman filter equations:

$$\begin{aligned} \hat{\mathbf{S}}_k &= \hat{\mathbf{S}}_k^- + \mathbf{K}_k \left(y_k - \hat{y}_k^- \right) \\ \mathbf{P}_{\mathbf{S}_k} &= \mathbf{P}_{\mathbf{S}_k}^- - \mathbf{K}_k \mathbf{P}_{\tilde{y}_k} \mathbf{K}_k^T . \end{aligned} \tag{27}$$

CHAPTER III

PHYSIOLOGICAL IMPULSE RESPONSE FUNCTION ESTIMATION AND CORRECTION TECHNIQUE: PIRFECT

3.1 Introduction

Physiological fluctuations due to respiration and cardiac pulsation are the dominant source of confounding variability in blood oxygenation level-dependent (BOLD) functional MRI (fMRI) at high field strengths [39, 30, 43]. It is vital to precisely characterize the impact of physiological events (single heart beat or breath) on the BOLD signal, so that it can be estimated and removed. Retrospective physiological noise correction techniques [39, 30] have been introduced to reduce short-term effects, having instantaneous impact on fMRI signal in concert with the respiratory and cardiac processes. The physiological sources of short-term cardiac pulse effects are tissue motion, CSF motion, large vessel pulsation, and changes in blood volume in the capillary bed [39, 19]. Short-term respiration effects result from head motion as well as B0 modulation due to bulk susceptibility changes from thoracic organ movement and gas volume [52, 39, 58, 57, 10, 64].

However, even after removing short-term effects using the retrospective techiques [39, 30], significant correlation between fMRI change and physiological change such as cardiac rate and respiratory volume change have been observed [65, 5, 60]. Breath-to-breath variation in respiratory volume leads to fluctuations in the carbon dioxide

(CO_2) content of arterial blood, a potent vasodilator. Cerebral blood flow fluctuations induced by these variations in CO_2 content result in low-frequency BOLD signal fluctuations throughout gray matter and near large vessels [65]. Respiration volume per time (RVT) has been proposed as an indicator of respiration induced signal fluctuations and has been shown to be significantly correlated with the BOLD signal [5]. These respiration induced fluctuations typically occur at a frequency of approximately 0.03 Hz [65, 5]. In addition, significant correlations between cardiac rate and BOLD signal fluctuations have been reported [60, 15]. While variations in respiration depth, respiration rate and heart rate are examples of sources of long-term effects, there are potentially other sources that have yet to be identified.

These studies indicate that existing retrospective techniques [39, 30] are inappropriate to remove long-term effects because they do not adequately characterize the noise contributions that span several physiological cycles. Previous works suggested including RVT and cardiac rate as nuisance regressors in general linear model (GLM) analyses [5, 60]. However, the physiological effects may not be limited to simple linear combinations of the RVT and cardiac rate time courses even though the both are correlated with the fMRI signal. In addition, estimating the voxel specific delay is challenging. Another method employs the respiration response function (RRF), which is the transfer function between RVT changes and BOLD signal change. To estimate the RRF, calibration scans in which subjects perform a single deep breath are performed and the BOLD signal acquired during this scan is averaged across brain voxels over several subjects [7] and used in the estimation. While this approach models the temporal shape of respiration effects, it assumes that the response of a single controlled breath precisely models the BOLD response of respiration. This may be the reason why the RRF model has a better goodness of fit to the controlled breathing task data than the resting state data. Furthermore, the RRF used earlier

[7] did not account for spatial and inter-subject variability.

Long-term physiological effects are particularly detrimental in resting-state functional connectivity analysis since their frequency range overlaps with the frequencies of fluctuations believed to reflect resting brain activity. Recent studies have shown significant correlations between the long-term physiological signal change and fMRI throughout gray matter, impeding detection of resting-state networks [6, 16]. Furthermore, studies have shown that the spatial distribution of the respiration long-term effects coincide with the default mode network [6].

Here, I describe an alternative approach to precisely model and remove physiological fluctuations from fMRI signal, physiological impulse response function estimation and correction (PIRFECT). A physiological impulse response function (PIRF), that is subject- and voxel-specific, is used to characterize how physiological events are translated into BOLD signal. The estimation of PIRF does not require a calibration scan. Once the PIRF is known it is used to generate a time course of physiological noise that is then removed from the data. PIRFECT is based on relative physiological timing information such as respiration and cardiac cycles and generalizes the retrospective techniques [39, 30] by relaxing the duration of physiological effects.

3.2 Theory

3.2.1 Model of Physiological Fluctuation

The retrospective physiological motion correction techniques described previously [39, 30] assume that physiological motion effects are pseudo-periodic and that their duration is limited to single physiological cycle. In this work, I generalized theses retrospective techniques by relaxing the duration of the physiological motion effect and including long-term effects that last several physiological cycles.

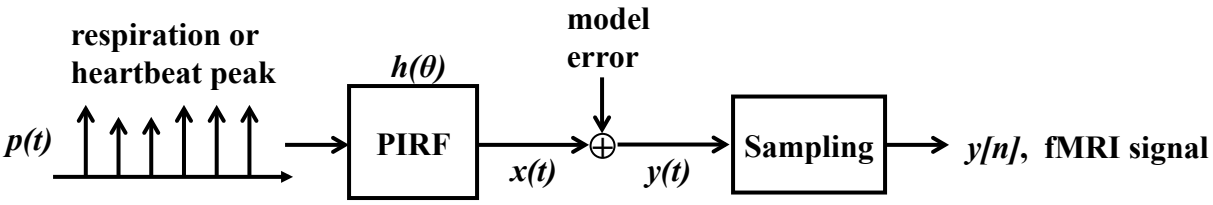

Figure 8: Schematic representation of time series of a voxel in fMRI signal in the reduced PIRFECT model

I first examine a reduced PIRFECT model including only one of physiological fluctuations. For a physiological impulse train $p(t)$, the impulse locations correspond to cycle epochs (i.e., the time of maximum inspiration or the R-wave peak) and magnitude is the cycles depth of respiration or 1 for heart beat. As shown in Fig. 8, the time series of a voxel in fMRI signal, $y(t)$, is modeled as the modeled physiological fluctuations with an unknown PIRF and a residual:

$$\begin{aligned} y(t) &= x(t) + e(t) \\ &= p\left(\theta(t)\right) * h\left(\theta(t)\right) + e(t) \end{aligned} \tag{28}$$

where $x(t)$ represents the modeled physiological signal change, $\theta(t)$ is the relative

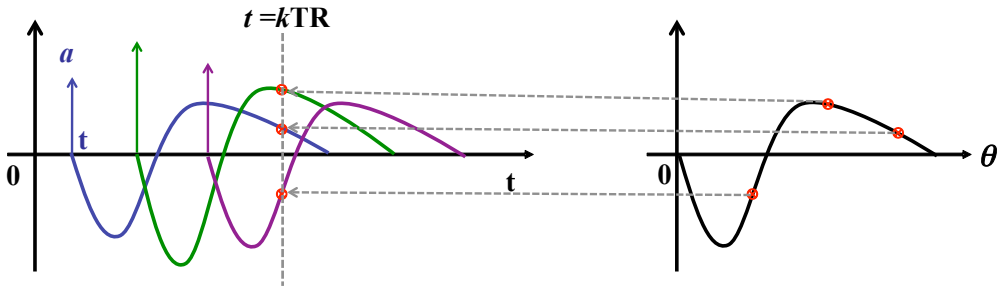

Figure 9: Illustration of model of long-term respiration fluctuations. Each impulse represents respiration epoch and magnitude represents the depth of respiration. Assuming the PIRF (to be estimated) is given as right plot, each respiration event contribute differently to fMRI signal at time $t = k\text{TR}$ depending on relative cycle.

cycle of physiological process, t represents the time at which data point is measured, $h(\theta)$ is the PIRF to be estimated, $*$ represents convolution, and $e(t)$ represents model error including other signal fluctuations. In this formalism, the previous retrospective techniques [39, 30] estimate a PIRF, $h(\theta)$, for one physiological cycle (i.e., $\{\theta : 0 \leq \theta \leq 1\}$) using a Fourier basis set. I generalize this idea from one to several cycles to account for long-term effects. Therefore, the long-term effects, such as fluctuations in BOLD signal due to breath-to-breath variations and heart rate variations, which are not modeled in previous techniques [39, 30], are modeled here. For the kth timepoint, the physiological signal change $x(k\text{TR})$ is modeled by a linear combination of scaled and time delayed instances of the PIRF.

$$x(k\text{TR}) = \sum_{\{i \,|\, p < \theta_i(k\text{TR})\}} a_i \, h\left(\theta_i(k\text{TR})\right), \tag{29}$$

where $\theta_i(k\text{TR}) = \frac{k\text{TR}-t_i}{t_{i+1}-t_i}$, t_i represents the time of i^{th} epoch, p and q denote the limits of the support of a PIRF $h(\theta)$ and TR represents the sampling period of $y(t)$. A full PIRFECT model is described as a sum of short-term and long-term respiration fluctuation as well as both cardiac fluctuations as shown in Fig. 10. To increase model

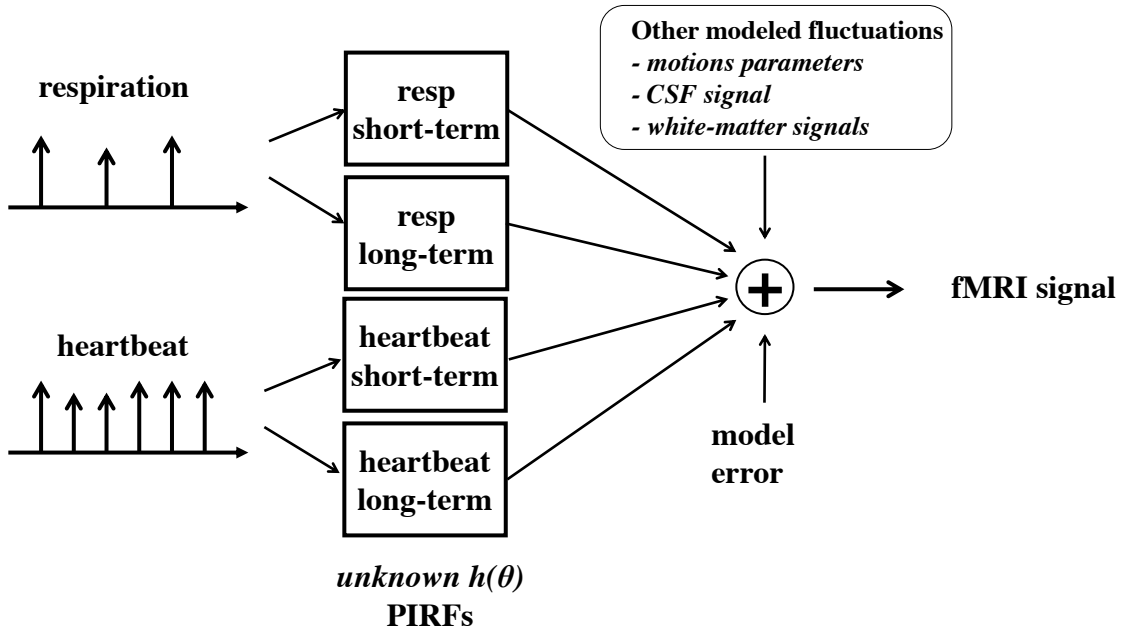

Figure 10: Schematic representation of time series of a voxel in fMRI signal in the full PIRFECT model

accuracy, other fluctuations, such as movement parameters, averaged white-mater and cerebrospinal fluid (CSF) regressors can be included in the model.

$$y(t) = x^S_{resp}(t) + x^L_{resp}(t) + x^S_{heart}(t) + x^L_{heart}(t) + o(t) + e(t) \tag{30}$$

where $x^S_{resp}(t)$ is short-term respiration fluctuations, $x^L_{resp}(t)$ is long-term respiration fluctuations, $x^S_{heart}(t)$ is short-term cardiac fluctuations, $x^L_{heart}(t)$ is long-term cardiac fluctuations, $o(t)$ is other modeled fluctuations, and plus model error, $e(t)$.

3.2.2 Estimation of Physiological Impulse Response

Without loss of generality, a reduced PIRFECT model is used to describe a estimation of PIRF. By dividing the compact support of a PIRF h(θ) into M bins (where M is equal to or less than the number of time points N), we can express the ideal physiological signal in a matrix-vector form as follows:

$$\mathbf{x} = \mathbf{A}\mathbf{h} \tag{31}$$

where $\mathbf{x} = [x(1 \times \mathrm{TR}),\, x(2 \times \mathrm{TR}),\, \ldots\, , x(N \times \mathrm{TR})]^T$ and the element a_{kj} of the $N \times M$ matrix $\mathbf{A}$ is the contribution of the physiological signal to the j^{th} bin of the PIRF at the k^{th} TR, and $\mathbf{h} = \left[h(1 \times \frac{p-1}{M}),\, x(2 \times \frac{p-1}{M}),\, \ldots\, , x(N \times \frac{p-1}{M})\right]^T$. Noisy fMRI measurements are expressed as:

$$\mathbf{y} = \mathbf{A}\mathbf{h} + \mathbf{r}, \tag{32}$$

where $\mathbf{y} = [y(1 \times \mathrm{TR}),\, y(2 \times \mathrm{TR}),\, \ldots\, , y(N \times \mathrm{TR})]^T$ and $\mathbf{e}$ denotes a $N \times 1$ error vector including model error and other signal fluctuations. Our goal is to estimate the PIRF $h(\theta)$ from the measured fMRI signal $\mathbf{y}$. Assuming independent zero mean Gaussian noise, the well-known maximum-likelihood (ML) estimator is

$$\hat{\mathbf{h}}_{\mathrm{ML}} = [\mathbf{A}^{\mathbf{T}}\mathbf{A}]^{-\mathbf{1}}\mathbf{A}^{\mathbf{T}}\mathbf{y}. \tag{33}$$

The matrix $\mathbf{A}^{\mathbf{T}}\mathbf{A}$ may be be ill-conditioned and the solution may be unstable. To overcome this problem, we will use a penalized-likelihood (PL) estimation which regularizes the solution. Specifically, we find $\mathbf{h}_{\mathrm{PL}}$ by minimizing the following cost functions:

$$\mathbf{\Psi}(\mathbf{h}) = -\log\, p(\mathbf{A}|\mathbf{h}) + \beta\, \mathbf{R}(\mathbf{h}) \tag{34}$$

The first term is the negative log-likelihood and the second term is a regularization penalty function in which β denotes the regularization parameter. The regularization penalty is formed from the observation that physiological signal variations occur at lower frequencies [65, 5, 60, 7, 15] and thus, a smooth PIRF is desirable. It is also assumed that the PIRF is zero at its boundaries. The smoothness condition and boundary condition are embodied in the following regularization penalty function:

$$\mathbf{R}(\mathbf{h}) = \frac{1}{2}(\mathbf{h}[1] - 0)^2 + \frac{1}{2}(\mathbf{h}[M] - 0)^2 + \sum_{n=2}^{M} \frac{1}{2}(\mathbf{h}[n] - \mathbf{h}[n-1])^2, \tag{35}$$

Assuming independent zero mean Gaussian noise, the solution of Eq. (34) is

$$\hat{\mathbf{h}}_{\mathrm{PL}} = [\mathbf{A^T A} + \beta\sigma^{\mathbf{2}}\mathbf{R}]^{-\mathbf{1}}\mathbf{A^T y}. \tag{36}$$

where σ^2 is the noise variance and the element R_{kj} of the $(M+1) \times M$ matrix $\mathbf{R}$ is

$$R_{kj} = 2\,\delta[k-j] + \delta[k-j-1] + \delta[k-j+1]. \tag{37}$$

Alternatively, one can estimate the PIRF $\mathbf{h}$ using a Fourier basis set as previously done [39, 30]. I express Eq. (31) as

$$\mathbf{x} = \mathbf{AFb} = \mathbf{Gb}, \tag{38}$$

where b denotes the $(2s+1) \times 1$ Fourier coefficients vector, s denote the order of Fourier series, and $\mathbf{F}$ represents the $M \times (2s+1)$ matrix form of Fourier basis:

$$\{F_{jk}\} = \begin{cases} \sin\left(2\pi\frac{j\cdot k}{q-p}\right), \text{if } j = 1, 3, 5, \cdots \\ \cos\left(2\pi\frac{j\cdot k}{q-p}\right), \text{if } j = 2, 4, 6, \cdots \end{cases}. \tag{39}$$

The ML estimator of Fourier coefficients $\hat{\mathbf{b}}$ is given by

$$\hat{\mathbf{b}} = [\mathbf{G^T G}]^{-1}\mathbf{G^T y}. \tag{40}$$

In this approach, the previous retrospective techniques [39, 30] are the special case when $p = 0$ and $q = 1$.

Once the PIRF is estimated from Eq. (36) or Eq. (40), the correction is performed on a voxel-by-voxel basis by removing the estimated physiological effects from measurement based on Eq. (31) or Eq. (38). Instead, the correction can be made by inclusion of the $(2s + 1)$ physiological regressors, $\mathbf{G}\hat{\mathbf{b}}$ in GLM analyses as nuisance covariates, as well as other covariates such as the motion parameters, for the Fourier basis approach.

3.3 Methods

3.3.1 Image acquisition

Eleven healthy volunteers participated in this study after giving informed consent in accordance with Georgia Institute of Technology's Institutional Review Board. All MRI experiments were conducted on a 3T Siemens Tim Trio scanner (Siemens Medical Solutions, Malvern, PA) equipped with a twelve-channel head coil. Anatomic images were acquired with a 3D T1-weighted magnetization-prepared rapid gradient echo imaging (MPRAGE) sequence (FOV = 256×256×176 mm^3, resolution 1×1×1 mm^3, TR = 2250 ms, TE = 3.98 ms, flip angle = 9°). Resting state data were acquired using a T2*-weighted echo-planar imaging sequence with the following parameters: 148-volumes, FOV = 204 × 204 mm^2, matrix = 68 × 68, 37 interleaved axial slices with 17 % gap, thickness = 3 mm, TE = 30 msec, flip angle = 90°, generalized auto-calibrating partially parallel acquisition (GRAPPA) imaging with an acceleration factor of 2 while the subjects were inactive (lying still with a visual fixation cross projected onto the screen).

3.3.2 Physiological recording

All physiological recording was performed using an integrated Siemens Physiological Monitoring Unit. During functional scans, the cardiac signal was monitored with a pulse oximeter placed on a finger of subjects, which provides a delayed systolic signal as well as the oxygenation saturation level. Respiratory signal was monitored with a flexible pressure belt placed around the upper abdomen of subjects. The sampling frequency of all physiological recording was 50 Hz.

3.3.3 Data Preprocessing

Resting-state scans were preprocessed using AFNI (`http://afni.nimh.nih.gov/afni/`) for most of the data analysis. In addition, FSL (`http://www.fmrib.ox.ac.uk/fsl/`) was used for brain segmentation and registration. The first four volumes of each run were discarded to remove T1 saturation effects. the data were corrected for motion by aligning each volume to the mean image volume using Fourier interpolation in AFNI. Then the data were spatially smoothed using a 5-mm FWHM Gaussian kernel. Mean-based intensity normalization was done by scaling all volumes by the same factor (10,000). The data were temporally filtered using both a high-pass (Gaussian-weighted least squares straight- line fitting, with $\sigma = 100.0s$) and low-pass (Gaussian low-pass temporal filtering, with a HWHM of 2.8 s) filter, followed by linear detrending to remove any residual drift. After the skull was removed using AFNI, registration of each individuals high-resolution anatomic image to a common stereotactic space [the Montreal Neurological Institutes 152-brain template (MNI152); 3 mm isotropic voxel size] was done using a 12degrees of freedom linear affine transformation (FLIRT) in FSL toolbox. The resulting transformation was then applied to each individuals functional dataset.

3.3.4 Models of Physiological Effects

The PIRFECT technique was performed with in-house MATLAB (MathWorks, Natick, MA) routines. Short-term physiological effects were modeled using Fourier basis with $p = 0$, $q = 1$ and $s = 2$. This approach is equivalent to RETROICOR [30]. Previous study [7] showed that fMRI signal change with respect to a breath-hold challenge was characterized as a bimodal response with an early signal increase, peaking at 3 s, followed by a pronounced undershoot of even greater magnitude, peaking at 16 s and returning to baseline at 40 s. With average respiration cycle of 4 s, long-term

respiratory effects were modeled with $p = 0$, $q = 9$ and $s = 3$ resulting the best goodness-of-fit on preliminary data. Long-term cardiac effects were modeled with $p = 0$, $q = 20$ and $s = 3$ based on the cardiac response function [15].

For each subject, physiological fluctuations were removed voxel-wise from the data via multiple regression. The full PIRFECT model consists of short-term and long-term respiratory effects as well as short-term and long-term cardiac effects. In the regression model, additional regressors are included as nuisance signals including white matter (WM), cerebrospinal fluid (CSF), and six motion parameters. The WM and CSF covariates were generated by segmenting each individuals high-resolution structural image (using FAST in FSL). The resulting segmented WM and CSF images were thresholded to ensure 80% tissue type probability. These thresholded masks were then applied to each individuals time series, and a mean time series was calculated by averaging across time series of all voxels within each mask. The six motion parameters were calculated in the motion-correction step during preprocessing. Movement in each of the three cardinal directions (X, Y, and Z) and rotational movement around three axes (pitch, yaw, and roll) were included for each individual. The variance explained by the long-term effects was computed using an R^2-test.

3.4 Results

The estimated respiration signal change was highly correlated with RVT change delayed by 2 second (see Fig. 11). This result agrees well with a previous study [65, 5] and demonstrates that the proposed method accurately estimated the respiration induced signal change. Maps depicting the percent signal variance explained at each voxel for the long-term PIRFECT model are shown for 3 subjects in Fig. 12. For all subjects, the long-term PIRFECT model explained significant variance over some extent of the brain. The PIRFs exhibit significant regional variations as expected. Unlike the transfer function method [7] which uses a separate calibration scan to estimate the average response of deep breaths in the entire brain, the PIRF described here is estimated from the dataset itself, voxel-by-voxel without separate calibration dataset.

It is not known whether a single averaged respiration response function such as Birn's RRF [7] can serve as a representative mapping of each voxels. Subject averaged respiratory PIRF were computed for each as well as global averaged one for all subjects in voxels reached significance ($p < 0.01$, uncorrected) by a F-test. The Pearson correlation coefficient (CC) between average PIRFs and each PIRFs for suprathreshold voxels were calculated (Fig. 13). With subject average PIRFs, means of CC varied substantially across the subjects (min: 0.25 and max: 0.68). The ratio of standard deviations to the means of CC was large (average ratio 1.14) indicating spatial variability in respiration PIRF shape. With global average PIRF, means of CC was smaller than with subject average. This suggests that there is substantial subject variability as well as spatial variability. Large standard deviations (average 0.46) with small means of CC (average 0.18) support that global respiration PIRF may not be a good representation of other PIRFs.

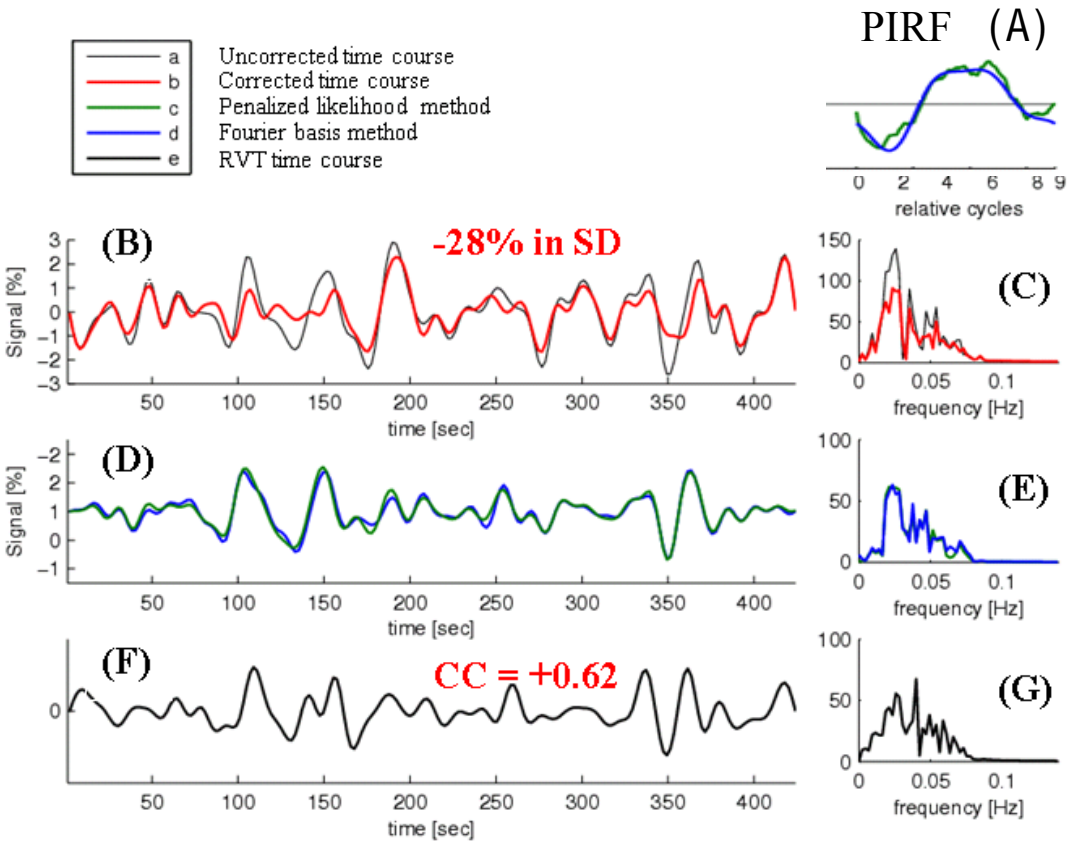

Figure 11: An example: (A) The estimated PIRF of respiration from a representative voxel in a representative subject. (B) fMRI time courses. The standard deviation is reduced by 28% (D) The estimated respiration-related fluctuations. (F) The 2 second delayed RVT. The correlation between the estimated signal and 2 second delayed RVT is positively high ($CC = +0.62$). (C, E, and G) Fourier transforms of time courses in panel B, D, and F respectively. Black: uncorrected time course after band-passed filtering (0.009 Hz $< f <$ 0.08 Hz), Red: corrected time course with band-filtering. The correction is made before filtering. Blue: Fourier basis method, Green: penalized likelihood method and Bold black: RVT time course.

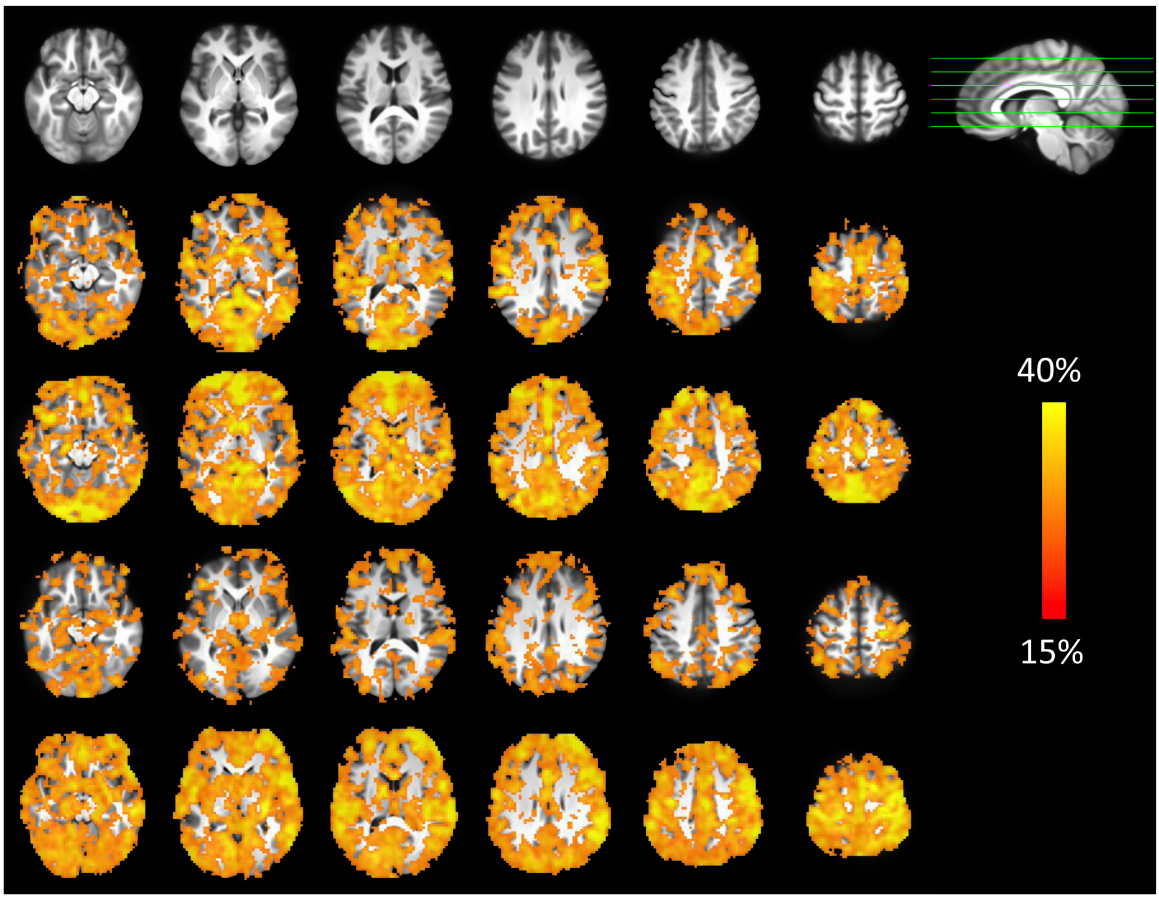

Figure 12: Maps of the percent signal variance explained by the long-term PIRFECT model for 4 subjects.

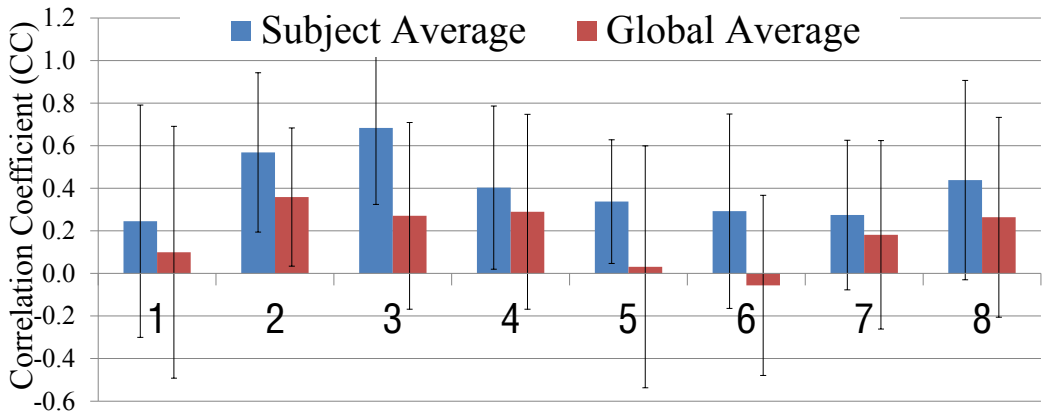

Figure 13: Means and standard deviations of Pearson correlation coefficients (CC); with subject average PIRF (blue) and global average PIRF (red)

To examine space and subject variability of long-term respiration effects by clustering the voxel-specific PIRFs, K-means clustering, based on using sample correlation as distance measure, was performed on voxels in which the respiratory components reached significance ($p < 0.01$, uncorrected) by a F-test from eight subjects using 5 clusters (Fig. 14). The average and standard deviation of PIRFs were calculated for each cluster (Fig. 15). To compensate for inter-subject variability in BOLD signal change, the signal was normalized before taking the average. Supra-threshold voxels were located in mostly grey matter. There are overlapped areas in supra-threshold voxels across the subjects. However, the patterns of the clusters varied substantially across subjects. Cluster A and B were the most dominant components (23% and 26% respectively). However, other clusters (D and E) were the most dominant in some subjects (4, 6 and 8). The substantial variation in the average cluster PIRFs indicates the spatial and subject variability of respiration artifacts. The small standard deviations of the average PIRFs show that clusters are relatively tight.

To test the effectiveness of removing the breath-to-breath variations, I compared the correlations between the BOLD signal and delayed RVT changes for uncorrected and corrected datasets. The RVT changes were obtained by dividing the difference between the maximum and minimum belt positions by the time between the maximum belt positions (the respiration period) and filtering this raw time course using low pass filter (f < 0.1 Hz) as described by Birn et al [5]. The correlation maps were generated and converted to Z-maps. The correlations between the resting-state fMRI time courses and delayed RVT changes are substantially reduced in the corrected dataset (see Fig. 16), demonstrating that the PIRFECT significantly reduced non-neuronal BOLD signal variations.

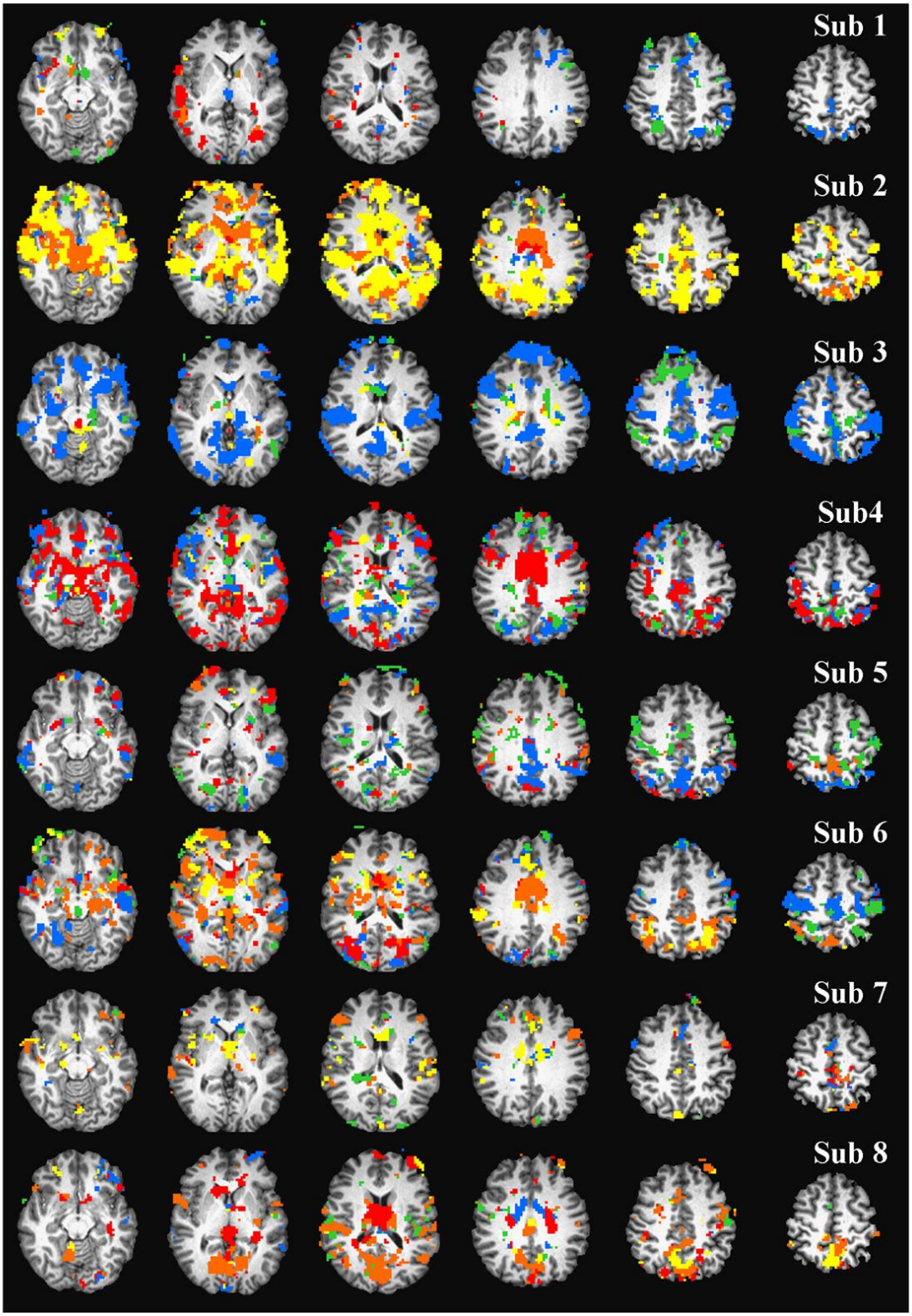

Figure 14: Clustering of respiration PIRFs in 6 slices in 8 subjects. Each row represents a subject. Each cluster represents in a different color

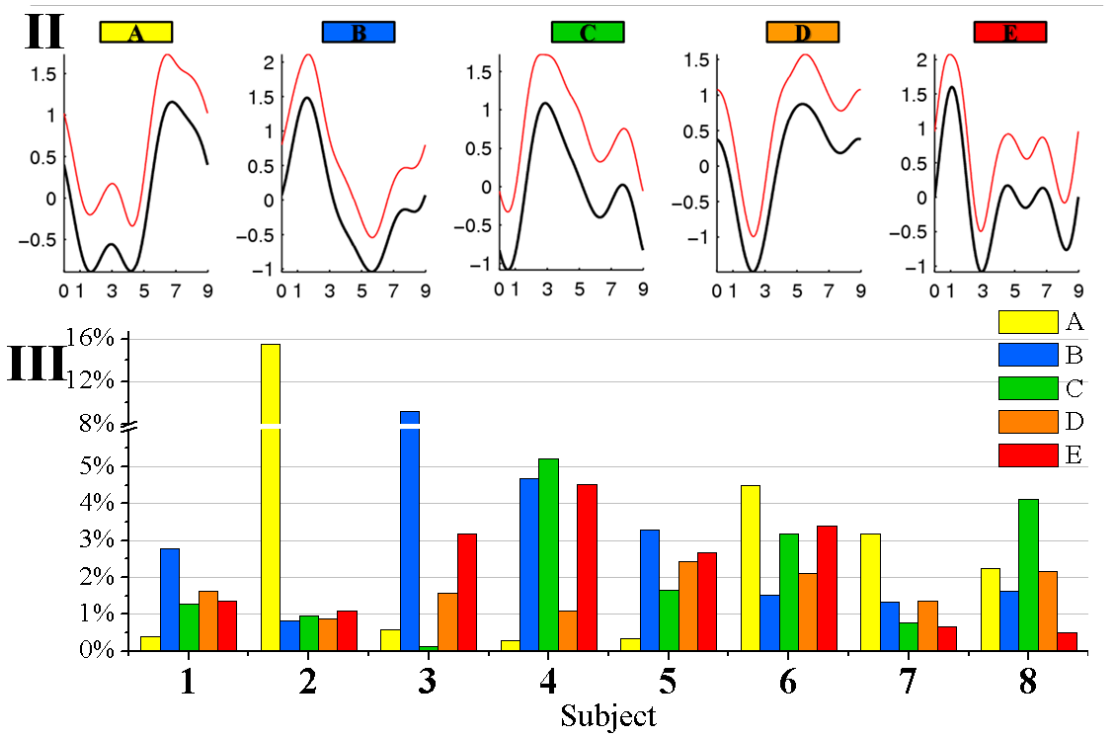

Figure 15: (top) Average PIRFs of each cluster (black line) and one standard deviation (red line). (bottom) Percentage of each cluster per a subject shown in Fig 14

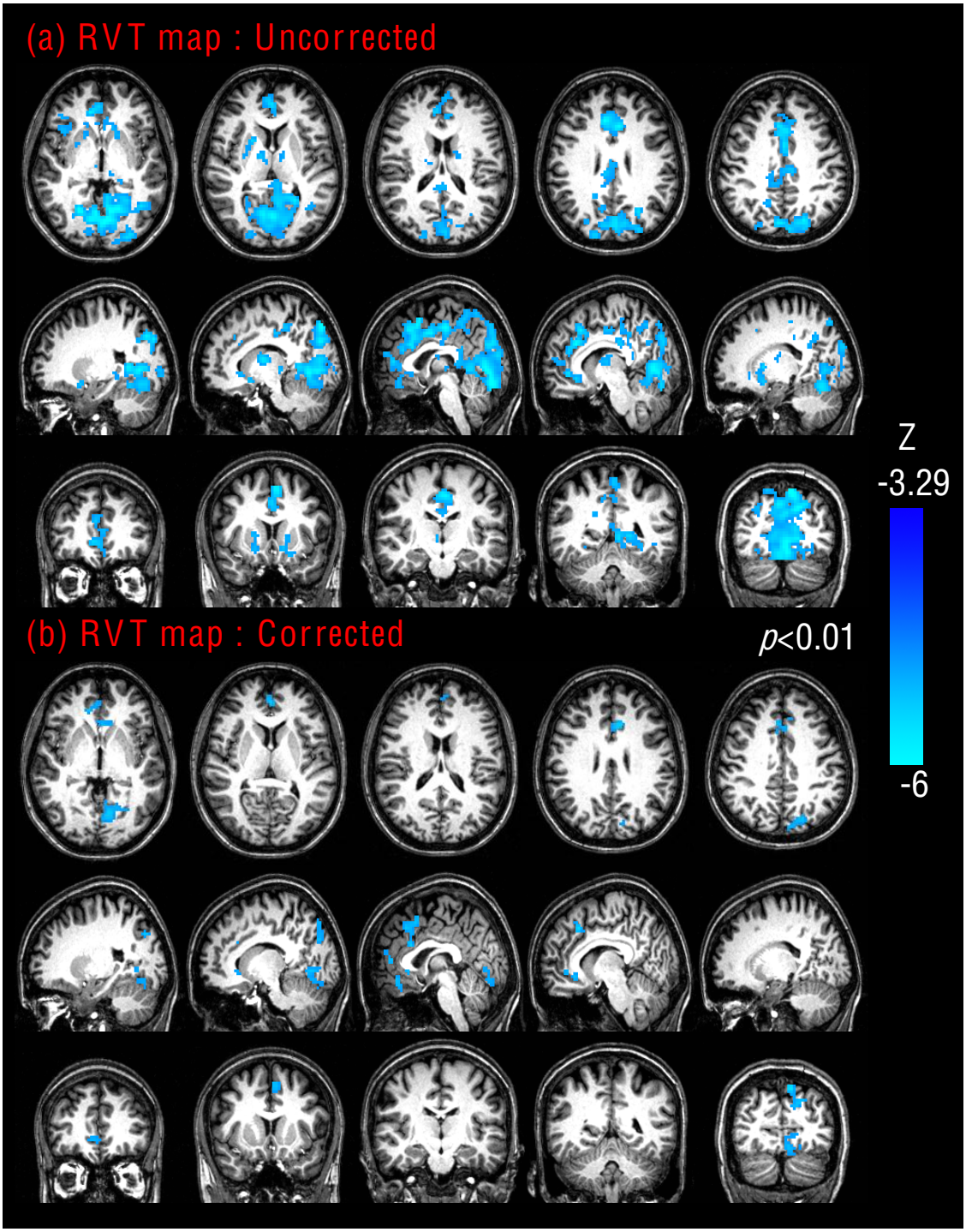

Figure 16: Maps representing significant correlated with respiration volume per time (RVT) changes (A) before and (B) after long-term PIRFECT correction

3.5 Discussion

Previous studies have found significant correlation between the BOLD signal and respiration volume change and heart rate [65, 5, 60, 7, 6, 15]. In this work, I assume that 1) BOLD signal response to the physiological event (single heart beat and breath) lasts longer than a single physiological cycle and 2) this response is voxel specific and subject dependent. With these assumptions, a generalized retrospective correction technique, PIRFECT, is introduced and demonstrated with respiration and cardiac effects.

It has been observed that the BOLD signal is highly correlated with external physiological monitored signals, including RVT, the partial pressure of end-tidal carbon dioxide and heart rate [65, 5, 60, 7, 6, 15]. Nonetheless, the retrospective techniques proposed earlier [39, 30, 43] are not successful in removing these fluctuations. It can be explained in the PIRFECT framework. If single physiological event has the long-term (e.g. 30 sec) fMRI response, several neighborhood events simultaneously contribute to fMRI signals at each time point. Therefore, the fluctuations in respiration and heart rate would lead to fluctuations in fMRI signal due to varying cumulative effects of several neighborhood events. The existing techniques [39, 30] estimate the instantaneous fMRI response within single physiological cycle, do not address the overlapping effects from multiple cycles and cannot correct the long-term fluctuations.

In estimating PIRF, I observe regional variability across the brain. On the other hand, I also found that adjacent regions have similar PIRFs. The long-term respiration fluctuations are likely related to carbon dioxide, a potent cerebral vasodilator

[65] although the precise physiological origin is unclear at this point. The BOLD signal results from complicated contributions from cerebral blood flow, metabolism and brain vasculature. It is not surprising that the physiological effects are region-specific and subject-specific.

The regularization and Fourier basis method yield smooth PIRF. The smoothness leads to physiologically plausible solution and prevents unacceptably noisy solution due to over-fitting [31, 14]. This is one of reasons why a previous direct deconvolution approach failed to obtain a reliable response function [7]. The resolution property of penalized likelihood estimation can be found in a review [22]. An advantage of Fourier basis approach is that it can be integrated into the GLM analysis as nuisance regressors using routinely available fMRI analysis tools. More importantly, this approach enables PIRFECT flexible to use and can improve estimation accuracy and the validity of the drawn inferences by including confounding effects such as motion, mean WM/CSF regressors in the GLM analysis [49]. The implicit assumption of PIRFECT is that long-term physiological fluctuations are not correlated with the neuronal signal changes. If this assumption is violated, PIRFECT may remove signals of interest as well as physiological fluctuations. This may be particularly a concern in brain regions involving the control of respiration and heart beat. Also, because PIRFECT employs a linear time-invariant (in sense that the physiological change depends on the relative cycles despite of physiological period) system approach, it is difficult to model irregular physiological effects such as breath-holding and sudden increase in the depth of breathing.

The PIRFECT approach estimates the voxel-specific physiological response without the need of a separate calibration scan. The reliability of these estimates can be gauged by the goodness-of-fit. It should be noted that the goodness-of-fit here

needs to be interpreted with caution because BOLD signal variations that arise not from respiration or heart beat are considered as error in the fit. Thus, it is not always true that a "reliable" estimate lead to a "good fit." The present study employs regularization in PIRF estimation to avoid over-fit and to obtain physiologically plausible response. In present study, the RVT is used as independent measured signal to supplement a reliability of estimate in agreement with previous study [5].

The PIRFECT method is a generalization of retrospective techniques. First of all, the duration of physiological effects is allowed to be longer than a single cycle and its starting time is also flexible. The physiological cycle instead of the absolute time is used to estimate PIRF in this sense. Unlike instantaneous physiological effects, long-term fluctuations are expected to take some time to develop. This flexible starting time lag can be included in PIRFECT model to increase estimation accuracy and to reduce residual instantaneous effects.

CHAPTER IV

EFFECT OF PHYSIOLOGICAL FLUCTUATIONS ON RESTING-STATE NETWORKS

4.1 Introduction

Along with the rapid growth of methods and applications of functional brain mapping for localizing regions with specialized functions, there has been a great deal of interest and progress made in studying brain connectivity. In particular, neuroimaging data can be used to infer functional connectivity which permits a systematic understanding of brain activity and allows the establishment and validation of network models of various brain functions. With the advent of functional neuroimaging, approaches have been developed to probe functional connectivity [44]. One approach for examining connectivity, that has gained a great deal of interest, is based on the temporal correlations in functional neuroimaging data [27]. Functional connectivity has been defined as "temporal correlations between spatially remote neurophysiological events [27]." With fMRI data acquired during the absence of an explicit task, i.e., the resting-state [24, 11], low-frequency time course fluctuations were found to be temporally correlated between functionally related areas. These low frequency oscillations seem to be a general property of symmetric cortices and/or relevant regions, have been shown to exist in a number of brain networks [36, 8, 9, 48] and have been revealed with data-driven analysis approaches [18, 56]. These fluctuations agree with the concept of functional connectivity defined by Friston et al. [27]. Several such sets of temporally correlated regions, known as resting-state networks (RSNs), can be identified consistently across human subjects [3, 20, 12]. and are presumed to reflect a basic functional organization of the brain. While the mechanism of interregional

correlation in resting state fluctuations is not well understood, this correlation may be due to strengthened synaptic connections between areas with synchronized electrical activity, in accordance with Hebb's theory [38]. Several recent studies have shown decreased low frequency correlations for patients in pathological states, including cocaine use [46], cerebral and Alzheimer's disease [47]. Thus, low frequency functional connectivity provides an important characterization of the brain. Interestingly, there seems to be a concordance between connectivity identified from baseline data and that identified from data acquired during a continuous task [36]. Several signal-processing techniques may be employed to delineate functional connectivity [45]. Of these, seed-based correlation and independent component analysis (ICA) exemplify two of the most frequently-used classes of methods. In seed-based correlation, one computes an index of temporal similarity such as Pearson correlation between one region of interests (ROI) and all other voles in the brain [32, 8]. Other techniques have been proposed for resting-state network such as independent component analysis (ICA) [4] and self-organizing maps [56].

However, non-neural physiological fluctuations arising from respiratory and cardiac processes are particularly detrimental in resting-state functional connectivity analysis since their frequency range overlaps with the frequencies of fluctuations believed to reflect resting brain activity. Recent studies have shown significant correlations between the long-term physiological signal change and fMRI throughout gray matter, impeding detection of resting-state networks [6, 16]. Furthermore, studies have shown that the spatial distribution of the respiration long-term effects coincide with the default mode network [6]. This chapter seeks to characterize the effects of physiological fluctuations on resting-state networks.

4.2 Methods

4.2.1 Image acquisition

Eleven healthy volunteers participated in this study after giving informed consent in accordance with Georgia Institute of Technology's Institutional Review Board. All MRI experiments were conducted on a 3T Siemens Tim Trio scanner (Siemens Medical Solutions, Malvern, PA) equipped with a twelve-channel head coil. Anatomic images were acquired with a 3D T1-weighted magnetization-prepared rapid gradient echo imaging (MPRAGE) sequence (FOV = 256×256×176 mm^3, resolution 1×1×1 mm^3, TR = 2250 ms, TE = 3.98 ms, flip angle = 9°). Resting state data were acquired using a T2*-weighted echo-planar imaging sequence with the following parameters: 148-volumes, FOV = 204 × 204 mm^2, matrix = 68 × 68, 37 interleaved axial slices with 17 % gap, thickness = 3 mm, TE = 30 msec, flip angle = 90°, generalized auto-calibrating partially parallel acquisition (GRAPPA) imaging with an acceleration factor of 2 while the subjects were inactive (lying still with a visual fixation cross projected onto the screen).

4.2.2 Physiological recording

All physiological recording was performed using an integrated Siemens Physiological Monitoring Unit. During functional scans, the cardiac signal was monitored with a pulse oximeter placed on a finger of subjects, which provides a delayed systolic signal as well as the oxygenation saturation level. Respiratory signal was monitored with a flexible pressure belt placed around the upper abdomen of subjects. The sampling frequency of all physiological recording was 50 Hz.

4.2.3 Data Preprocessing

Resting-state scans were preprocessed using AFNI (`http://afni.nimh.nih.gov/afni/`) for most of the data analysis. In addition, FSL (`http://www.fmrib.ox.ac.uk/fsl/`) was used for brain segmentation, registration, and Independent Component Analysis (ICA). The first four volumes of each run were discarded to remove T1 saturation effects. the data were corrected for motion by aligning each volume to the mean image volume using Fourier interpolation in AFNI. Then the data were spatially smoothed using a 5-mm FWHM Gaussian kernel. Mean-based intensity normalization was done by scaling all volumes by the same factor (10,000). The data were temporally filtered using both a high-pass (Gaussian-weighted least squares straight-line fitting, with $\sigma = 100.0s$) and low-pass (Gaussian low-pass temporal filtering, with a HWHM of 2.8 s) filter, followed by linear detrending to remove any residual drift. After the skull was removed using AFNI, registration of each individual's high-resolution anatomic image to a common stereotactic space [the Montreal Neurological Institute's 152-brain template (MNI152); 3 mm isotropic voxel size] was done using a 12-degrees of freedom linear affine trans- formation (FLIRT) in FSL toolbox. The resulting transformation was then applied to each individual's functional dataset.

Physiological fluctuations removal

Consistent with common practice in the resting-state fMRI literature [49, 5, 7, 15, 16, 63], nuisance signals were removed from the data via multiple regression before functional connectivity analyses were performed. This step is designed to control for the effects of physiological processes, such as fluctuations related to motion and cardiac and respiratory cycles. The common regressors include white matter (WM), cerebrospinal fluid (CSF), and six motion parameters. The WM and CSF covariates

were generated by segmenting each individual's high-resolution structural image (using FAST in FSL). The resulting segmented WM and CSF images were thresholded to ensure 80% tissue type probability. These thresholded masks were then applied to each individual's time series, and a mean time series was calculated by averaging across time series of all voxels within each mask. The six motion parameters were calculated in the motion-correction step during preprocessing. Movement in each of the three cardinal directions (X, Y, and Z) and rotational movement around three axes (pitch, yaw, and roll) were included for each individual.

Besides the common regressors, the physiological fluctuations are modeled in 6 different ways to examine the effect of physiological noise correction on the RSNs. For each subject, 6 types of time series were derived with multiple linear regression: 1) No correction, 2) reduced PIRFECT model (only short-term effects equivalent to RETROICOR [30]) consisting of 4 respiratory regressors and 4 cardiac regressors using Fourier basis up to 2nd orders, 3) full PIRFECT model (both short-term and long-term effects) consisting of 8 short-term regressors and additional 12 regressors for long-term effects using Fourier basis up to 3rd orders, 4) short-term regressors and global signal regressor generated by averaging across the time series of all brain voxels, and 5) 8 short-term regressors and two long-term regressors described by Birn et al [7] for respiratory effects (RV) and by Chang et al [15] for cardiac effects (HR). The each individual's residual 4D time series data were spatially normalized by applying the previously computed transformation to the MNI152 standard space.

4.2.4 Impact on resting-state networks

Seed-based correlation analysis

The each individual's 4D time series were divided into two sessions of 4D time series using the half of time points to evaluate the intra-session reproducibility of RSNs.

Two session datasets were processed identically to delineate RSNs. Three 5-mm-radius seed regions of interest (ROIs) centered on the coordinates previously used by [63] were created to examine functional connectivity for each of three regions. The ROIs were located in the posterior cingulate cortex (PCC; MNI Coordinate 0, -53, 26), the right primary visual cortex (V1; 30, -88, 0), and the right primary motor cortex (M1; 36, -25, 57). Then the time series for each seed was extracted from these data. Time series were averaged across all voxels in each seed's ROI. For each session dataset, the correlation between the time series of the seed ROI and that of each voxel in the brain was determined. This analysis was implemented using 3dfim+ (AFNI) to produce individual-level correlation maps of all voxels that were positively or negatively correlated with the seed's time series. For each subject, two correlation maps were compared with the correlation coefficient.

Group ICA and dual regression

To gauge the influence of long-term physiological removal by PIRFECT on RSNs in the group ICA, dual regression [23] allowing for voxel-wise comparisons of resting functional connectivity, was performed between two groups of datasets before and after long-term physiological noise correction. Short-term physiological fluctuations are modeled and removed. This approach proceeds in 3 stages. First, the concatenated multiple fMRI data sets are decomposed using ICA to identify large-scale patterns of functional connectivity in the population of subjects. In this analysis, the data set was decomposed into 11 components, in which the model order was estimated using the Laplace approximation to the Bayesian evidence for a probabilistic principal component model. RSNs of interest were selected using spatial correlation against a set of three maps from seed-based correlation analysis. Second, the dual-regression approach is used to identify, within each subject's fMRI data set, subject-specific

temporal dynamics and associated spatial maps. This involves (i) using the full set of group-ICA spatial maps in a linear model fit (spatial regression) against the separate fMRI data sets, resulting in matrices describing temporal dynamics for each component and subject, and (ii) using these time-course matrices in a linear model fit (temporal regression) against the associated fMRI data set to estimate subject-specific spatial maps. Finally, the different component maps are collected across subjects into single 4D files (1 per original ICA map, with the fourth dimension being subject identification) and tested voxel-wise for statistically significant pair-wise differences between groups using nonparametric permutation testing (5,000 permutations) [51]. This results in spatial maps characterizing the between-group differences. These maps were thresholded using an alternative hypothesis test based on fitting a Gaussian/gamma mixture model to the distribution of voxel intensities within spatial maps and controlling the local false-discovery rate at $p < 0.05$.

4.3 Results

The functional connectivity map are presented after both short-term and long-term physiological noise correction (Fig. 17) with the posterior cingulate cortex (PCC), the primary visual cortex (V1), and the primary motor cortex (M1) as seed's ROIs. Application of short-term physiological noise correction yielded increased reproducibility of all three RSNs. Of different correction technique, the full PIRFECT model showed the highest mean correlation compared to the global signal model and the existing long-term model introduced by [7, 15]. Similar RSNs were identified using group ICA in Fig. 18 after full PIRFECT correction. After long-term physiological noise correction, the significant decreased coactivation were observed for all three RSNs at $p < 0.05$ (corrected).

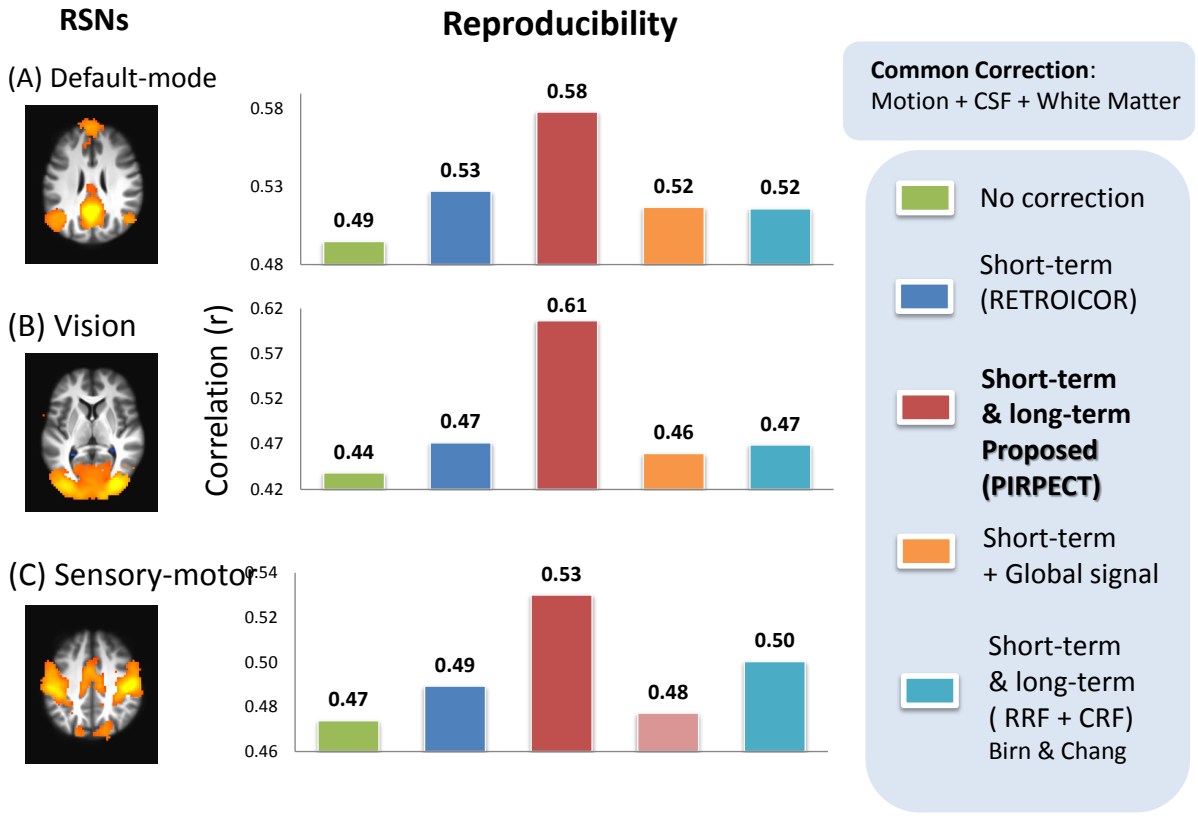

Figure 17: Effects of physiological noise corrections on the reproducibility of functional connectivity maps using seed-based correlation analysis: (left) functional connectivity maps with the posterior cingulate cortex (PCC), the primary visual cortex (V1), and the primary motor cortex (M1) as seed's ROI, (right) mean correlation coefficient across 11 subjects between functional connectivity maps from two intra-sessions

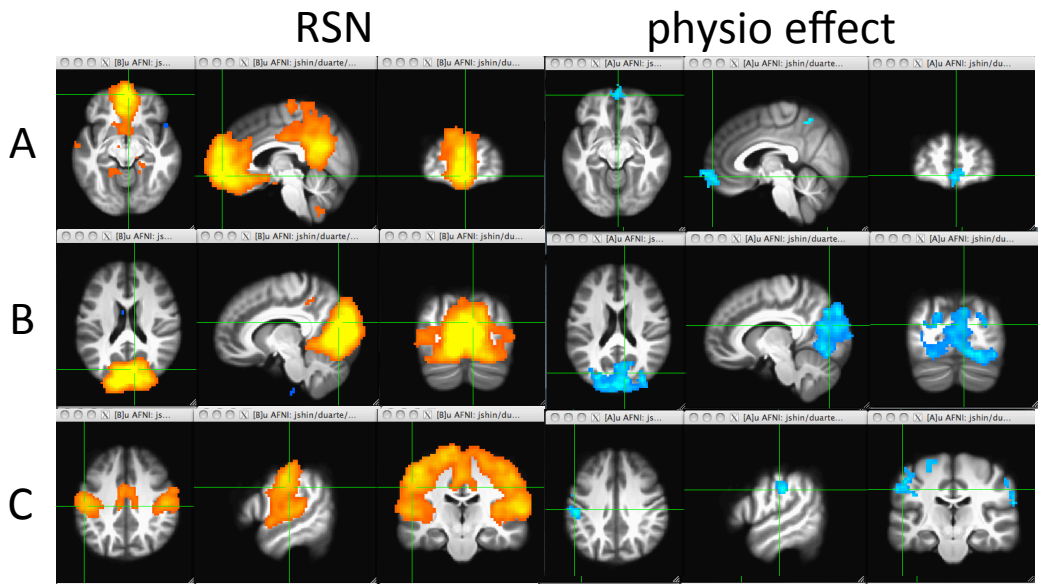

Figure 18: Impacts on resting-state networks using group ICA: (left) Group-level spatial maps representing (A) the default mode network, (B) the visual network, and (C) the sensory-motor network are identified. (right) RSNs comparison between the before and after long-term physiological fluctuations removal using PIRFECT revealed significantly decreased coactivation after removal ($p < 0.05$, corrected)

4.4 Discussion and Conclusions

This study indicates that low-frequency resting-state networks in fMRI are still present after short-term and long-term physiological noise correction with seed-based correlation analysis and ICA analysis. The reproducibility of RSNs has substantially increased after removing physiological fluctuations using full PIRFECT model, even higher than the global signal removal approach [24, 25] and the existing RVHR approach [7, 15]. These results suggest that physiological noise correction will be vital for fMRI resting-state functional connectivity study.

REFERENCES

[1] Bandettini, P. A., Jesmanowicz, A., Wong, E. C., and Hyde, J. S., "Processing strategies for time-course data sets in functional mri of the human brain," *Magnetic Resonance in Medicine*, vol. 30, no. 2, pp. 161–173, 1993.

[2] Bandettini, P. A., Wong, E. C., Hinks, R. S., Tikofsky, R. S., and Hyde, J. S., "Time course epi of human brain function during task activation," *Magn Reson Med*, vol. 25, no. 2, pp. 390–397, 1992.

[3] Beckmann, C. F., DeLuca, M., Devlin, J. T., and Smith, S. M., "Investigations into resting-state connectivity using independent component analysis," *Philos. Trans. R. Soc. Lond., B, Biol. Sci.*, vol. 360, no. 1457, pp. 1001–1013, 2005.

[4] Beckmann, C. F. and Smith, S. M., "Probabilistic independent component analysis for functional magnetic resonance imaging," *Medical Imaging, IEEE Transactions on*, vol. 23, no. 2, pp. 137–152, 2004.

[5] Birn, R. M., Diamond, J. B., Smith, M. A., and Bandettini, P. A., "Separating respiratory-variation-related fluctuations from neuronal-activity-related fluctuations in fmri," *Neuroimage*, vol. 31, pp. 1536–48, Jul 2006.

[6] Birn, R. M., Murphy, K., and Bandettini, P. A., "The effect of respiration variations on independent component analysis results of resting state functional connectivity," *Hum Brain Mapp*, vol. 29, pp. 740–50, Jul 2008.

[7] Birn, R. M., Smith, M. A., Jones, T. B., and Bandettini, P. A., "The respiration response function: the temporal dynamics of fmri signal fluctuations related to changes in respiration," *Neuroimage*, vol. 40, pp. 644–54, Apr 2008.

[8] Biswal, B., Yetkin, F. Z., Haughton, V. M., and Hyde, J. S., "Functional connectivity in the motor cortex of resting human brain using echo-planar mri," *Magn Reson Med*, vol. 34, no. 4, pp. 537–541, 1995.

[9] Biswal, B. B., Kylen, J. V., and Hyde, J. S., "Simultaneous assessment of flow and bold signals in resting-state functional connectivity maps," *NMR in Biomedicine*, vol. 10, no. 45, pp. 165–170, 1997.

[10] Brosch, J. R., Talavage, T. M., Ulmer, J. L., and Nyenhuis, J. A., "Simulation of human respiration in fmri with a mechanical model," *IEEE Trans Biomed Eng*, vol. 49, pp. 700–7, Jul 2002.

[11] Buckner, R. L. and Vincent, J. L., "Unrest at rest: default activity and spontaneous network correlations," *Neuroimage*, vol. 37, no. 4, pp. 1091–1096, 2007.

[12] Buckner, R., Andrews-Hanna, J., and Schacter, D., "The brain's default network," *Annals of the New York Academy of Sciences*, vol. 1124, no. 1, pp. 1–38, 2008.

[13] Buxton, R. B., Wong, E. C., and Frank, L. R., "Dynamics of blood flow and oxygenation changes during brain activation: the balloon model," *Magn Reson Med*, vol. 39, no. 6, pp. 855–864, 1998.

[14] Casanova, R., Ryali, S., Serences, J., Yang, L., Kraft, R., Laurienti, P. J., and Maldjian, J. A., "The impact of temporal regularization on estimates of the bold hemodynamic response function: a comparative analysis," *Neuroimage*, vol. 40, pp. 1606–18, May 2008.

[15] Chang, C., Cunningham, J. P., and Glover, G. H., "Influence of heart rate on the bold signal: the cardiac response function," *Neuroimage*, vol. 44, pp. 857–69, Feb 2009.

[16] Chang, C. and Glover, G. H., "Effects of model-based physiological noise correction on default mode network anti-correlations and correlations," *Neuroimage*, vol. 47, pp. 1448–59, Oct 2009.

[17] Chen, W., Zhu, X. H., Thulborn, K. R., and Ugurbil, K., "Retinotopic mapping of lateral geniculate nucleus in humans using functional magnetic resonance imaging," *Proc Natl Acad Sci USA*, vol. 96, pp. 2430–2434, Mar 1999.

[18] Cordes, D., Haughton, V., Carew, J. D., Arfanakis, K., and Maravilla, K., "Hierarchical clustering to measure connectivity in fmri resting-state data," *Magnetic resonance imaging*, vol. 20, no. 4, pp. 305–317, 2002.

[19] Dagli, M. S., Ingeholm, J. E., and Haxby, J. V., "Localization of cardiac-induced signal change in fmri," *Neuroimage*, vol. 9, pp. 407–15, Apr 1999.

[20] Damoiseaux, J. S., Rombouts, S., Barkhof, F., Scheltens, P., Stam, C. J., Smith, S. M., and Beckmann, C. F., "Consistent resting-state networks across healthy subjects," *Proc Natl Acad Sci USA*, vol. 103, no. 37, pp. 13848–13853, 2006.

[21] DuBois, R. M. and Cohen, M. S., "Spatiotopic organization in human superior colliculus observed with fmri," *Neuroimage*, vol. 12, pp. 63–70, Jul 2000.

[22] Fessler, J. A. and Rogers, W. L., "Spatial resolution properties of penalized-likelihood image reconstruction: space-invariant tomographs," *IEEE Trans Image Process*, vol. 5, no. 9, pp. 1346–58, 1996.

[23] Filippini, N., MacIntosh, B. J., Hough, M. G., Goodwin, G. M., Frisoni, G. B., Smith, S. M., Matthews, P. M., Beckmann, C. F., and Mackay, C. E., "Distinct patterns of brain activity in young carriers of the apoe-ε4 allele," *Proc Natl Acad Sci USA*, vol. 106, no. 17, pp. 7209–7214, 2009.

[24] Fox, M. D. and Raichle, M. E., "Spontaneous fluctuations in brain activity observed with functional magnetic resonance imaging," *Nature Reviews Neuroscience*, vol. 8, no. 9, pp. 700–711, 2007.

[25] Fox, M. D., Zhang, D., Snyder, A. Z., and Raichle, M. E., "The global signal and observed anticorrelated resting state brain networks," *Journal of neurophysiology*, vol. 101, no. 6, pp. 3270–3283, 2009.

[26] Fox, P. T. and Raichle, M. E., "Focal physiological uncoupling of cerebral blood flow and oxidative metabolism during somatosensory stimulation in human subjects," *Proc Natl Acad Sci USA*, vol. 83, no. 4, pp. 1140–1144, 1986.

[27] Friston, K. J., Frith, C. D., Liddle, P. F., Frackowiak, R. S. J., and others, "Functional connectivity: the principal-component analysis of large (pet) data sets," *J Cereb Blood Flow Metab*, vol. 13, no. 1, pp. 5–14, 1993.

[28] Friston, K. J., Glaser, D. E., Henson, R. N. A., Kiebel, S., Phillips, C., and Ashburner, J., "Classical and bayesian inference in neuroimaging: applications," *Neuroimage*, vol. 16, no. 2, pp. 484–512, 2002.

[29] Friston, K. J., Williams, S., Howard, R., Frackowiak, R. S. J., and Turner, R., "Movement-related effects in fmri time-series," *Magnetic resonance in medicine*, vol. 35, no. 3, pp. 346–355, 1996.

[30] Glover, G. H., Li, T. Q., and Ress, D., "Image-based method for retrospective correction of physiological motion effects in fmri: Retroicor," *Magn Reson Med*, vol. 44, pp. 162–167, Jul 2000.

[31] Goutte, C., Nielsen, F. A., and Hansen, L. K., "Modeling the haemodynamic response in fmri using smooth fir filters," *IEEE Trans Med Imaging*, vol. 19, pp. 1188–201, Dec 2000.

[32] Greicius, M. D., Krasnow, B., Reiss, A. L., and Menon, V., "Functional connectivity in the resting brain: a network analysis of the default mode hypothesis," *Proc Natl Acad Sci U S A*, vol. 100, pp. 253–8, Jan 2003.

[33] Griffiths, T. D., Uppenkamp, S., Johnsrude, I., Josephs, O., and Patterson, R. D., "Encoding of the temporal regularity of sound in the human brainstem," *Nat Neurosci*, vol. 4, pp. 633–637, Jun 2001.

[34] Guimaraes, A. R., Melcher, J. R., Talavage, T. M., Baker, J. R., Ledden, P., Rosen, B. R., Kiang, N. Y. S., Fullerton, B. C., and

Weisskoff, R. M., "Imaging subcortical auditory activity in humans," *Hum Brain Mapp*, vol. 6, no. 1, pp. 33–41, 1998.

[35] Haacke, E. M., Brown, R. W., Thompson, M. R., and Venkatesan, R., *Magnetic resonance imaging: physical principles and sequence design*, vol. 82. Wiley-Liss New York:, 1999.

[36] Hampson, M., Peterson, B. S., Skudlarski, P., Gatenby, J. C., and Gore, J. C., "Detection of functional connectivity using temporal correlations in mr images," *Human brain mapping*, vol. 15, no. 4, pp. 247–262, 2002.

[37] Havlicek, M., Friston, K. J., Jan, J., Brazdil, M., and Calhoun, V. D., "Dynamic modeling of neuronal responses in fmri using cubature kalman filtering," *NeuroImage*, vol. 56, no. 4, pp. 2109 – 2128, 2011.

[38] Hebb, D., *The organization of behavior: A neuropsychological theory*. Lawrence Erlbaum, 2002.

[39] Hu, X., Le, T. H., Parrish, T., and Erhard, P., "Retrospective estimation and correction of physiological fluctuation in functional mri," *Magn Reson Med*, vol. 34, pp. 201–212, Aug 1995.

[40] Jiru, F. and Klose, U., "Fast 3d radiofrequency field mapping using echo-planar imaging," *Magn Reson Med*, vol. 56, pp. 1375–1379, Dec 2006.

[41] Julier, S. J. and Uhlmann, J. K., "Unscented filtering and nonlinear estimation," *Proceedings of the IEEE*, vol. 92, no. 3, pp. 401–422, 2004.

[42] Kalman, R. E., "A new approach to linear filtering and prediction problems," *Journal of basic Engineering*, vol. 82, pp. 35–45, 1960.

[43] Krüger, G. and Glover, G. H., "Physiological noise in oxygenation-sensitive magnetic resonance imaging," *Magn Reson Med*, vol. 46, pp. 631–7, Oct 2001.

[44] Lee, L., Harrison, L. M., and Mechelli, A., "A report of the functional connectivity workshop, dusseldorf 2002," *NeuroImage*, vol. 19, no. 2, pp. 457–465, 2003.

[45] Li, K., Guo, L., Nie, J., Li, G., and Liu, T., "Review of methods for functional brain connectivity detection using fmri," *Computerized Medical Imaging and Graphics*, vol. 33, no. 2, pp. 131–139, 2009.

[46] Li, S. J., Biswal, B., Li, Z., Risinger, R., Rainey, C., Cho, J. K., Salmeron, B. J., and Stein, E. A., "Cocaine administration decreases functional connectivity in human primary visual and motor cortex as detected by functional mri," *Magn Reson Med*, vol. 43, no. 1, pp. 45–51, 2000.

[47] Li, S. J., Li, Z., Wu, G., Zhang, M. J., Franczak, M., and Antuono, P. G., "Alzheimer disease: Evaluation of a functional mr imaging index as a marker1," *Radiology*, vol. 225, no. 1, pp. 253–259, 2002.

[48] Lowe, M. J., Mock, B. J., and Sorenson, J. A., "Functional connectivity in single and multislice echoplanar imaging using resting-state fluctuations," *Neuroimage*, vol. 7, pp. 119–32, Feb 1998.

[49] Lund, T. E., Madsen, K. H., Sidaros, K., Luo, W.-L., and Nichols, T. E., "Non-white noise in fmri: does modelling have an impact?," *Neuroimage*, vol. 29, pp. 54–66, Jan 2006.

[50] Lutti, A., Hutton, C., Finsterbusch, J., Helms, G., and Weiskopf, N., "Optimization and validation of methods for mapping of the radiofrequency transmit field at 3t," *Magn Reson Med*, vol. 64, pp. 229–238, Jul 2010.

[51] Nichols, T. E. and Holmes, A. P., "Nonparametric permutation tests for functional neuroimaging: a primer with examples," *Human brain mapping*, vol. 15, no. 1, pp. 1–25, 2002.

[52] Noll, D. and Schneider, W., "Theory, simulation, and compensation of physiological motion artifacts in functional mri," in *Image Processing, 1994. Proceedings. ICIP-94., IEEE International Conference*, vol. 3, pp. 40–44, IEEE, 1994.

[53] Ogawa, S., Lee, T. M., Kay, A. R., and Tank, D. W., "Brain magnetic resonance imaging with contrast dependent on blood oxygenation," *Proc Natl Acad Sci USA*, vol. 87, no. 24, p. 9868, 1990.

[54] Ogawa, S., Lee, T. M., Nayak, A. S., and Glynn, P., "Oxygenation-sensitive contrast in magnetic resonance image of rodent brain at high magnetic fields," *Magn Reson Med*, vol. 14, no. 1, pp. 68–78, 1990.

[55] Ogawa, S., Tank, D. W., Menon, R., Ellermann, J. M., Kim, S. G., Merkle, H., and Ugurbil, K., "Intrinsic signal changes accompanying sensory stimulation: functional brain mapping with magnetic resonance imaging," *Proc. Natl. Acad. Sci. U.S.A.*, vol. 89, no. 13, p. 5951, 1992.

[56] Peltier, S. J., Polk, T. A., and Noll, D. C., "Detecting low-frequency functional connectivity in fmri using a self-organizing map (som) algorithm," *Human brain mapping*, vol. 20, no. 4, pp. 220–226, 2003.

[57] Raj, D., Anderson, A. W., and Gore, J. C., "Respiratory effects in human functional magnetic resonance imaging due to bulk susceptibility changes," *Phys Med Biol*, vol. 46, pp. 3331–40, Dec 2001.

[58] Raj, D., Paley, D. P., Anderson, A. W., Kennan, R. P., and Gore, J. C., "A model for susceptibility artefacts from respiration in functional echoplanar magnetic resonance imaging," *Phys Med Biol*, vol. 45, pp. 3809–20, Dec 2000.

[59] Schneider, K. A., Richter, M. C., and Kastner, S., "Retinotopic organization and functional subdivisions of the human lateral geniculate nucleus:

a high-resolution functional magnetic resonance imaging study," *J Neurosci*, vol. 24, pp. 8975–8985, Oct 2004.

[60] Shmueli, K., van Gelderen, P., de Zwart, J. A., Horovitz, S. G., Fukunaga, M., Jansma, J. M., and Duyn, J. H., "Low-frequency fluctuations in the cardiac rate as a source of variance in the resting-state fmri bold signal," *Neuroimage*, vol. 38, pp. 306–20, Nov 2007.

[61] Thulborn, K. R., Waterton, J. C., Matthews, P. M., and Radda, G. K., "Oxygenation dependence of the transverse relaxation time of water protons in whole blood at high field," *Biochimica et Biophysica Acta (BBA)-General Subjects*, vol. 714, no. 2, pp. 265–270, 1982.

[62] van Der Merwe, R., *Sigma-point Kalman filters for probabilistic inference in dynamic state-space models*. PhD thesis, Oregon Health & Science University, 2004.

[63] Van Dijk, K. R. A., Hedden, T., Venkataraman, A., Evans, K. C., Lazar, S. W., and Buckner, R. L., "Intrinsic functional connectivity as a tool for human connectomics: theory, properties, and optimization," *Journal of neurophysiology*, vol. 103, no. 1, pp. 297–321, 2010.

[64] Windischberger, C., Langenberger, H., Sycha, T., Tschernko, E. M., Fuchsjäger-Mayerl, G., Schmetterer, L., and Moser, E., "On the origin of respiratory artifacts in bold-epi of the human brain," *Magn Reson Imaging*, vol. 20, pp. 575–82, Oct 2002.

[65] Wise, R. G., Ide, K., Poulin, M. J., and Tracey, I., "Resting fluctuations in arterial carbon dioxide induce significant low frequency variations in bold signal," *Neuroimage*, vol. 21, pp. 1652–64, Apr 2004.